Protein aggregation and membrane bending govern nanotube morphology

H. Alimohamadi[1], B. Ovryn[2] and P. Rangamani*[1]

[1]Department of Mechanical and Aerospace Engineering, University of California San Diego, CA 92093, USA
[2]Department of Electrical and Computer Engineering, Colorado State University, CO 80523, USA

July 20, 2018

Abstract Membrane nanotubes have been identified as a dynamic way for cells to connect and interact over long distances. These long and thin membranous protrusions have been shown to serve as conduits for the transport of proteins, organelles, viral particles, and mRNA. Nanotubes typically appear as thin and cylindrical tubes, but they can also have a beads-on-a-string architecture. Here, we study the role of membrane mechanics in governing the architecture of these tubes and show that the formation of a bead-like structure along the nanotube can result from a local heterogeneity in the membrane due to protein aggregation or due to membrane composition. We present numerical results that predict how membrane properties, protein density, and tension compete to create a phase space that governs the morphology of a nanotube. We also find that the stability of multiple beads is regulated by an energy barrier that prevents two beads from fusing. These results suggest that the membrane-protein interaction, protein aggregation, and membrane tension closely regulate the tube radius, number of beads, and the bead morphology.

Keyword Membrane nanotubes, Lipid bilayer, Membrane curvature, Helfrich energy, Protein aggregation.

Introduction

Cell-cell communication is fundamental for material and information exchange in multicellular organisms and has been studied for many decades. Various mechanisms for short range communication have been reported including plasmodesmata in plant cells [1, 2], gap junctions in animal cells [3], and synapses in nervous systems [4–6]. Membrane nanotubes, also referred as tunneling nanotubes have been identified as intercellular structures that connect cells over long distances, i.e., hundreds of micrometers (see Fig.1) [7, 8], providing a highway for the transfer of small molecules, organelles, cargoes, mitochondria [9], and mRNA [10]. Membrane nanotubes have been observed in a wide variety of cell types such as epithelial cells, fibroblasts, neurons, and immune cells [8, 11–13]. Artificial nanotubes have also been produced from lipid vesicles [8, 14]. Although questions remain regarding the mechanisms governing nanotube formation, elongation, and fusion of the plasma membranes between the two connected cells, it is clear that the role played by membrane tension and heterogeneities along the nanotube remains poorly understood.

Membrane nanotubes are typically long and thin cylindrical protrusions with sub-micron diameters and lengths on the order of several hundred microns [7]. In contrast to other types of cellular projections, such as filopodia or endocytic invaginations, which are attached to the substrate and are often function specific [15–17], nanotubes are suspended in the medium and participate in a wide variety of cellular functions including embryonic development [18], calcium-mediated signal transduction [19], spreading of pathogens [13], spinal cord injuries [20], and even in

*prangamani@ucsd.edu

the development of some types of cancers [21]. Additionally membrane nanotubes are thought to mediate cell-cell communication via electrical, chemical, and mechanical signals [22].

Membrane nanotubes are dynamic structures and any microscopic change in the surrounding environment, rearrangement of membrane lipid or protein constituents, or external mechanical stresses can result in dramatic shape transformations [7, 23–26]. For instance, in addition to the predominant cylindrical geometry of many membrane nanotubes, the formation of bead like shapes along membrane nanotubes has been observed in various experiments [27, 28]. While the molecules involved and the biochemical reactions underneath the morphological transition in nanotubes structures have been the focus of many studies [29–32], the mechanical aspects have not been explored broadly. It has been proposed that the formation of the beads along membrane nanotubes could be the result of any lipid bilayer asymmetry such as protein-induced spontaneous curvature [24, 28, 33]. Although general relationships between the bead radius, nanotube radius, and the distance between beads for both area difference elastic (ADE) and spontaneous curvature models have been proposed [20], there are many unanswered questions. For example, tension also plays an important role in modulating the morphology of the nanotube and pearling of a membrane tube can be explained by a tension-driven Rayleigh-type instability [34–36]. Furthermore, recent papers showed both experimentally and theoretically that the change in the membrane shape in response to the protein-induced spontaneous curvature is accompanied by a change in the local tension of the membrane [37–41].

This study of the mechanisms that govern the formation of bead like structures on membrane nanotubes is motivated by our experimental observations of stable, well-defined beads on membrane nanotubes in living cells (Fig. 1A and B). We examine the role of membrane mechanics in governing these structures and their morphological transitions, and we address open questions about how membrane-protein interactions and membrane properties regulate the formation, maintenance, and morphology of membrane nanotubes. In this study, we seek to answer the following questions: How does membrane heterogeneity affect the shape of a nanotube? How does membrane-protein aggregation alter the morphology of a nanotube? What is the phase space that governs these morphological transitions of membrane nanotubes? To answer these questions, we used an augmented Helfrich model including the protein density contribution [42–45] with local incompressibility constraints [39, 46] to performed simulations.

Model Development

Assumptions

The plasma membrane is a complex structure; various molecules pack tightly together to form an semi impermeable shield barrier for the cytoplasm, nucleus and intercellular organelles [4]. However, under some assumptions, described below, we can model this complex and heterogeneous surface using a simpler mathematical framework to identify some fundamental principles.

- The length scale of the nanotube is assumed to be much larger (~ 20 times) than the thickness of the bilayer. Based on this assumption, we model the membrane as a thin elastic shell [45, 47, 48].
- We assume that the membrane nanotube is at mechanical equilibrium (i.e. no inertia) [49]. Also, because of the high stretching modulus of lipid bilayers [50], we assume that the lipid bilayer is areally incompressible. We use a Lagrange multiplier to implement this constraint [51, 52].
- We assume that the total energy of the system includes the membrane bending energy and a contribution from membrane-protein aggregation in a dilute regime. Thus, the membrane is modeled using an augmented version of Helfrich energy for elastic manifolds including the membrane-protein interaction contributions [42, 53–56]. The aggregation energy of the proteins, which is proportional to the gradient of the protein density, is modeled in our system by a hyperbolic tangent function. A detailed discussion of the full energy can be found in [56]. We do not explicitly model the diffusion of these proteins and the dynamics of the domains in this study; rather we assume that diffusion has run its course and we are left with a protein heterogeneity on the surface. We vary this heterogeneity along the nanotube.

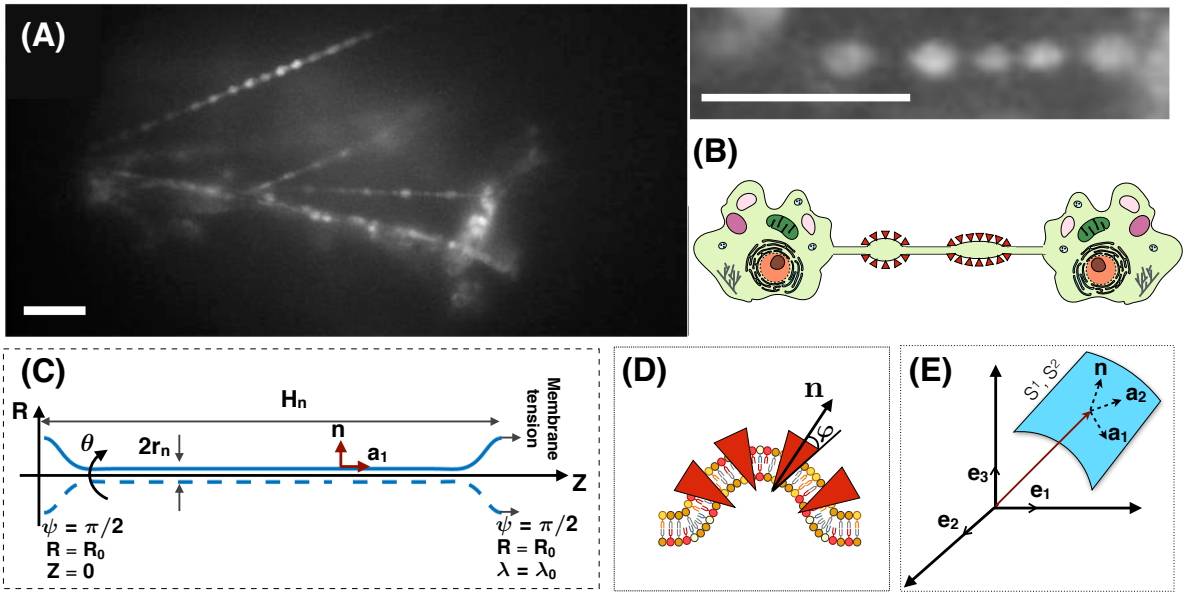

Figure 1: (A) Sialic acid labeled on glycoproteins on nanotubes with Alexa dye molecules on the surface of live (COS 7) cells. Scale bar is 5 microns [27]. (B) A cartoon showing an intercellular membrane nanotube with local bead-shaped deformations. (C) The axisymmetric modeling of the membrane nanotube and the applied boundary conditions are shown. (D) A schematic depicting membrane-protein interactions that could lead to the formation of beads along a nanotube. Proteins (shown in red) can aggregate along the membrane to induce local curvature and create a tension heterogeneity, which results in the formation of beads of various sizes and shapes. We assume the dispersed proteins to be cone-shaped such that their meridian makes an angle φ with the normal vector to the surface. (E) The coordinate system to define a surface by tangent basis $\mathbf{a_1}$, $\mathbf{a_2}$ and normal vector $\mathbf{n}$.

- We do not consider the role of forces applied by actin-mediated nanotube formation, so that we can focus only on membrane nanotube deformation due to membrane-protein interactions [57, 58].
- For simplicity in the numerical simulations, we assume that the membrane in the region of interest is rotationally symmetric (Fig. 1C).

Membrane energy and equations of motion

We model the membrane with two contributions to the strain energy – one from membrane-protein interactions and the other from membrane bending. The entropic interaction of transmembrane proteins with the lipid bilayer is written as a constitutive function of the protein density σ (number per unit area). While the exact form of this energy is yet to be experimentally verified, based on thermodynamic arguments, a quadratic dependence of the energy on the local protein density has been proposed as [42, 53, 56, 59, 60],

$$W_{\text{Protein}} = \alpha^2 \sigma(\theta^\xi)^2, \tag{1}$$

where W is the energy per unit area, and α^2 is an indicator of the membrane-protein interaction strength [56]. σ can depend explicitly on the surface coordinates θ^ξ ($\xi \in \{1,2\}$) to allow for local heterogeneity. Also, these proteins are assumed to be transmembrane, conical insertions such that the meridian of each protein is at an angle φ with the normal vector to the membrane surface (**n**) (See Fig. 1D). In the dilute regime, the local induced-spontaneous curvature due to membrane-protein interaction can be modeled as a linear function of the surface protein density as [43, 56]

$$C(\sigma) = \mu\varphi\sigma(\theta^\xi), \tag{2}$$

Table 1: Parameters used in the model

Notation	Description	Value
λ_0	Edge membrane tension [63, 64]	0 – 0.064 $\mathrm{pN/nm}$
κ_{lipid}	Bending rigidity of bare lipid membrane [65]	320 $\mathrm{pN \cdot nm}$
κ_{rigid}	Bending modulus of rigid domain [66–68]	320 – 9600 $\mathrm{pN \cdot nm}$
σ	Protein density [69]	0 – 2.5$\times 10^{-4}$ nm^{-2}
α	Protein aggregation strength [43]	3.57×10^3 $\mathrm{nm}^{1.5} \cdot \mathrm{pN}^{0.5}$
$\mu\varphi$	Constant length scale [43]	200 nm
A_{membrane}	Total area of the membrane	8π $\mu\mathrm{m}^2$
p	Transmembrane pressure	0 $\mathrm{pN/nm}^2$

where μ is a length scale that represents the lipid-protein specific entropic interactions. Other forms and relationships between spontaneous curvature and protein density are explored in [42].

The energy associated with membrane bending due to the spontaneous curvature is given by the Helfrich Hamiltonian, modified to include heterogeneous membrane properties as

$$W_{\text{Bending}} = \kappa(\theta^\xi)\left[H - C(\sigma(\theta^\xi))\right]^2 + \kappa_G(\theta^\xi)K, \tag{3}$$

where H is the local mean curvature, and K is the local Gaussian curvature. κ and κ_G are bending and Gaussian moduli respectively, which in the general case can vary along the surface coordinate θ^ξ [39, 61, 62]. Hence, the total energy of the membrane including both bending and protein contributions is given by

$$W(H, K, \sigma; \theta^\xi) = \underbrace{\kappa(\theta^\xi)\left[H - C(\sigma(\theta^\xi))\right]^2}_{\text{Bending}} + \underbrace{\kappa_G(\theta^\xi)K}_{\text{Gaussian}} + \underbrace{\alpha^2\sigma(\theta^\xi)^2}_{\text{Protein aggregation}} \tag{4}$$

Assuming that the membrane is at mechanical equilibrium at all times, we minimized the total energy using a stress balance approach [48], and solved the governing equations numerically. A complete derivation of all equations is provided in the SOM and the notation and values of parameters used in the model are summarized in Tables S1, S2, and S3.

Numerical implementation

In the axisymmetric coordinates, the equations of motion (Eq. S14 and Eq. S15) simplify to a system of first-order differential equations (Eq. (S26)) with six prescribed boundary conditions (Eq. (S27)). In order to solve these coupled equations, we used the commercially available finite element solver COMSOL MULTIPHYSICS ® 5.3. In this work, we assume that the total area of the membrane is conserved and to focus on the net effect of membrane tension, we set the transmembrane pressure at zero ($p = 0$).

Results

Heterogeneity in membrane properties can lead to formation of bead-like structures along a nanotube

For membrane nanotubes, it has been shown that the composition of the lipid bilayer is a critical factor in determining the shape and radius of nanotubes [70–72]. A change in lipid composition also corresponds to a change in membrane stiffness [70]. To understand how a heterogeneity in membrane properties due to lipid composition

affects the shape of a nanotube, we conducted simulations on cylindrical nanotubes with a significant aspect ratio of radius 35 nm and length 100 μm, and set the boundary tension to $\lambda_0 = 0.064$ pN/nm. The effect of boundary tension on the initial nanotube radius and length is shown in Figs. S1 and S2. On this nanotube, we prescribed a region of higher bending rigidity representing a change in the composition but not a change in the asymmetry between the leaflets. This defines a domain at the center of the nanotube that has a higher bending moduli with respect to the rest of the surface, with a rigidity ratio $\kappa_{\text{ratio}} = \kappa_{\text{rigid}}/\kappa_{\text{lipid}}$ [67, 72] (Fig. 2A). To have a smooth continuous transition, we implemented the difference in bending moduli using a hyperbolic tangent function Eq. (S28), such that the area of the rigid domain is fixed ($\text{A}_{\text{rigid}} = 1.6\pi\ \mu\text{m}^2$), and the bending rigidity ratio (κ_{ratio}) is varied between 1-30 [67, 72, 73]. With increasing κ_{ratio}, the membrane bends significantly in the area of the rigid segment and an ellipsoidal bead-shaped structure forms along the nanotube (Fig. 2B). For $\kappa_{\text{ratio}} < 10$, the radius of the bead increases almost linearly. However, for $\kappa_{\text{ratio}} > 10$ the size of the bead remains almost constant (Fig. 2B, inset). The local variation of membrane tension corresponding to the membrane bending in the beaded domain and the applied incompressibility constraint is shown in Fig. S3. For completeness, we also used a hyperbolic tangent function to parameterize a variation in the Gaussian modulus ($\Delta\kappa_G$) between -20 to 20. We found that the effect of varying Gaussian modulus alone leads to a very insignificant membrane deformation (see Fig S4).

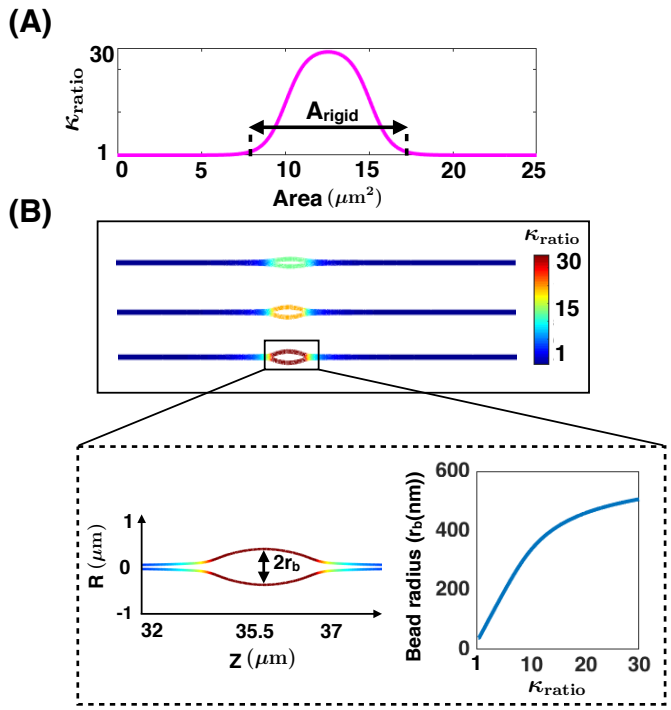

Figure 2: Heterogeneous membrane properties result in the formation of local bead-shaped structures (here $\sigma = 0$). (A) Bending modulus variation along the membrane surface in which $\text{A}_{\text{rigid}} = 1.6\pi\ \mu\text{m}^2$ represents the area of the localized rigid segment at the center of the nanotube, and κ_{ratio} shows the bending rigidity ratio of the rigid segment compared to that of the bare lipid membrane. (B) Membrane deformation in the region of large bending rigidity resembles a local bead formation phenomena; the tension at the boundary is set as $\lambda_0 = 0.064$ pN/nm. The inset shows the increase of the bead radius as a function of κ_{ratio}.

Beads formation along a nanotube due to membrane-protein interactions

Motivated by our numerical observation that a heterogeneity along the membrane can lead to bead-like structures, we next explored if localized surface protein aggregation could induce a similar deformation along the nanotube. To explore how protein domains can affect the tubular shape of a nanotube, we applied a distribution of the protein density – prescribed as a hyperbolic tangent function Eq. (S28) – along the surface of the elongated nanotube in

Fig. 1C with $\lambda_0 = 0.064\,\mathrm{pN/nm}$ and $\kappa_{\mathrm{ratio}} = 1$. Here, we assumed that the number of proteins per area increases ($\sigma_0 = 0$ to $\sigma_0 = 1.25 \times 10^{-4}\,\mathrm{nm}^{-2}$), while the area covered by the proteins at the center of the nanotube remains constant ($\mathrm{A}_{\mathrm{protein}} = 1.6\pi\,\mu\mathrm{m}^2$) (Fig. 3A). As shown in Fig. 3B, the membrane bends outward in the area of the protein aggregation in response to the protein-induced spontaneous curvature. As the number of proteins in the defined area is increased, the membrane deformation also increases such that it resembles a bead-shaped structure forming along the nanotube (Fig. 3B, inset). The local membrane tension distribution along the nanotubes and the bead-shaped structures is shown in Fig. S5.

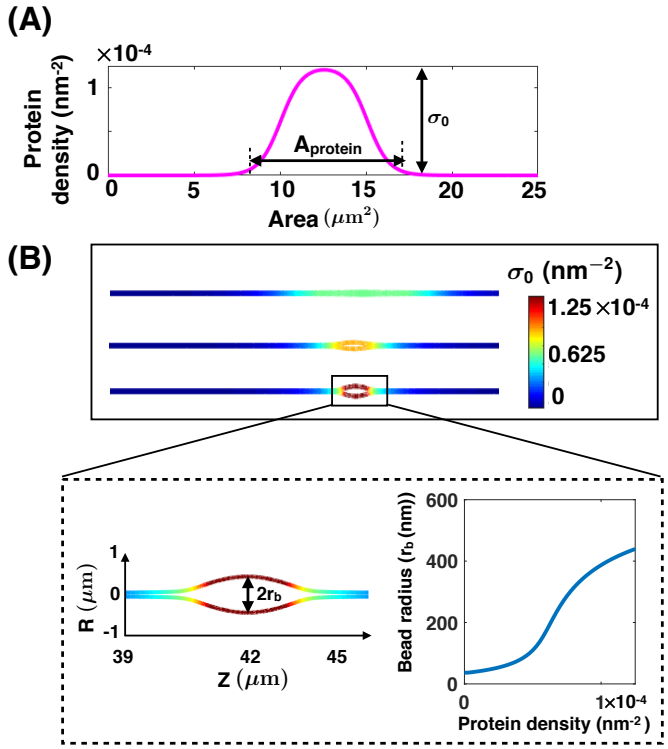

Figure 3: Protein-mediated bead formation along a membrane nanotube. (A) Protein density distribution on the membrane surface in which $\mathrm{A}_{\mathrm{protein}} = 1.6\pi\,\mu\mathrm{m}^2$ shows the area coverage of the protein-enriched domain and σ_0 represents the number of the proteins per unit area. (B) The formation of a large bead-shaped structure along the membrane nanotube while increasing the density of proteins per unit area (σ_0) for $\lambda_0 = 0.064\,\mathrm{pN/nm}$ and $\kappa_{\mathrm{ratio}} = 1$. The inset displays the increase of the bead radius as a function of the protein density.

Morphological landscape of bead-shaped structures along a nanotube

Thus far, simulation results demonstrate that two unrelated mechanisms, heterogeneity in membrane rigidity and protein-induced curvature, independently lead to formation of bead-like structures along the membrane nanotube. In order to explore how these two mechanisms might interact and modulate the shape of a nanotube, we conducted simulations where the heterogeneous domain has effects both from protein-induced spontaneous curvature and from increased bending rigidity. Initially, we repeated the simulations in Fig. 3 but this time assuming that $\kappa_{\mathrm{ratio}} = 11$. Interestingly, we found that the interaction of these two mechanisms leads to the formation of beads with different shapes. Based on the magnitude of the protein density, three different oblate spheroid shapes were obtained; *(i)* an ellipsoidal bead at $\sigma_0 = 0$, *(ii)* a flat cylindrical bead at $\sigma_0 = 4 \times 10^{-5}\,\mathrm{nm}^{-2}$, and *(iii)* a large unduloid-shaped bead at $\sigma_0 = 5.5 \times 10^{-5}\,\mathrm{nm}^{-2}$ (Fig. 4A). Thus, coupling the two modes of spatial heterogeneity along a membrane nanotube not only increases the radius of the bead (see Fig. S6) but also changes the shape of the bead. This shape transition suggests that the energy landscape of the membrane, which is now modulated by a heterogeneity in κ and a heterogeneity in σ, can lead to a range of shapes. To further identify over what range of protein

density and κ_{ratio} these shape transitions occur, we performed the same simulation over a range of protein densities, ($\sigma_0 = 0 - 2.5 \times 10^{-4}\,\text{nm}^{-2}$), as well as over a range of $\kappa_{\text{ratio}} = 1 - 11$, encompassing soft protein domains to very stiff clusters. This variation allowed us to construct a phase diagram to identify the regions of different bead morphologies (Fig. 4B). The red region represents the formation of ellipsoidal bead-shaped structures, the blue region denotes the cylindrical beads, and the green region indicates the unduloid-shaped beads configuration.

These changes of the bead morphology can be understood better by comparing the two "induced" length scales by the rigid domain ($\text{L}_\text{k} = 1/2\sqrt{\kappa_{\text{rigid}}/\lambda}$) [74] and the protein aggregation ($\text{L}_\sigma = 1/\mu\varphi\sigma$) [37, 46]. The "induced" length scale by the membrane-protein interaction $1/\mu\varphi\sigma$ is the preferred radius of curvature of the protein-enriched domain and increases with decreasing σ (with σ = 0, both spontaneous curvature and the effect of protein aggregation are eliminated). The phase diagram in Fig. 4B shows that these two length scales act in tandem to regulate the bead size and shape. In order to compare the length scales, we consider a case with a fixed value of L_k (e.g. $\kappa_{\text{ratio}} = 2$), and vary L_σ by increasing the protein density (Fig. 4B). First, we see that the ellipsoidal beads form for low protein density, *i.e.* when $\text{L}_\sigma \gg \text{L}_\text{k}$ (Fig. 4B). Second, the cylindrical beads are energetically favorable for average values of protein density when the two length scales become comparable ($\text{L}_\sigma \sim \text{L}_\text{k}$). Finally, at very large values of protein density, when the "induced" length scale by the rigid domain becomes dominant ($\text{L}_\text{k} \gg \text{L}_\sigma$), the unduloid-shaped bead forms along the nanotube (Fig. 4B).

Regardless of which mechanism dominates, the edge tension λ_0 implicitly governs the length scale of the membrane; therefore the natural question that arises is how does this tension govern the shape and length scale transitions of the beads? We explore these questions by conducting two sets of simulations. First, for a homogeneous membrane ($\kappa_{\text{ratio}} = 1$) we varied the edge membrane tension (λ_0) and protein density (σ_0) in a range ($\lambda_0 = 0.004 - 0.064\,\text{pN/nm}$ and $\sigma_0 = 0 - 2.5 \times 10^{-4}\,\text{nm}^{-2}$) (Fig. 4C). We observed that high edge tension shifted the transition of ellipsoidal to cylindrical and unduloid-shaped beads to large protein densities. Second, we fixed the protein density ($\sigma_0 = 6 \times 10^{-5}\,\text{nm}^{-2}$) and varied the edge tension (λ_0) and the rigidity ratio (κ_{ratio}) between 0.004- 0.064 pN/nm and 1-11 respectively (Fig. 4D). In this case, all three possible shapes of beads are accessible with varying the bending rigidity ratio. In fact, by increasing the edge membrane tension either at a constant protein density or a fixed rigidity ratio, we decreased the value of the the induced length scale by the rigid domain ($\sqrt{\kappa_{\text{rigid}}/\lambda}$) and moved from the cylindrical and unduloid-shaped beads to the ellipsoidal bead-shaped region of the phase space.

Interaction between multiple beads along a nanotube

Often, multiple stable beads are observed along a membrane nanotube, suggesting that multiple domains of heterogeneity exist along the nanotube [24, 27]. Using bioorthogonal click chemistry to label sialic acids on surface cell glycans in COS7 cells [27], a series of well defined and temporally stable bead structures along membrane nanotubes has been previously observed (Fig. 1A and B). These observations lead to the following question: how does the stability profile of these beaded strings depend on the different length scales associated with beaded nanotubes? In order to answer this question, we conducted simulations for the formation of two beads along the membrane by prescribing two areas of heterogeneity for three cases – (i) varying membrane rigidity alone in each domain in the absence of protein aggregation, (ii) varying protein density for uniform rigidity, and (iii) varying protein density for domains with different rigidity.

We first found when there are two regions of proteins far from each other with an end-to-end area given by $A_{\text{separation}} = 1.6\pi\ \mu\text{m}^2$ (Fig. 5A, top), two independent beads form (Fig. 5A bottom). The size and the shape of the beads are independent of the number of domains as long as the domains are far away from each other (Fig. S7 and Fig. S8). Having established that the regions of heterogeneity are independent when they are far from each other, we next asked under what conditions might these beads interact with one another? In other words, what length scales govern the stability features of multiple beads knowing there is a certain relaxation length between the beads and cylinder? To answer this question, we repeated the simulation of two beads by varying the rigidity ratio (κ_{ratio}) and end-to-end area ($A_{\text{separation}}$) between 1-11 and $0 - 1.6\pi\ \mu\text{m}^2$ respectively. Based on the results, we constructed a phase diagram separating the two possible morphologies; (*i*) two distinct beads represented by color blue, and (*ii*) one single bead denoted by color red (Fig. 5B). We found that when the two domains are bought together by

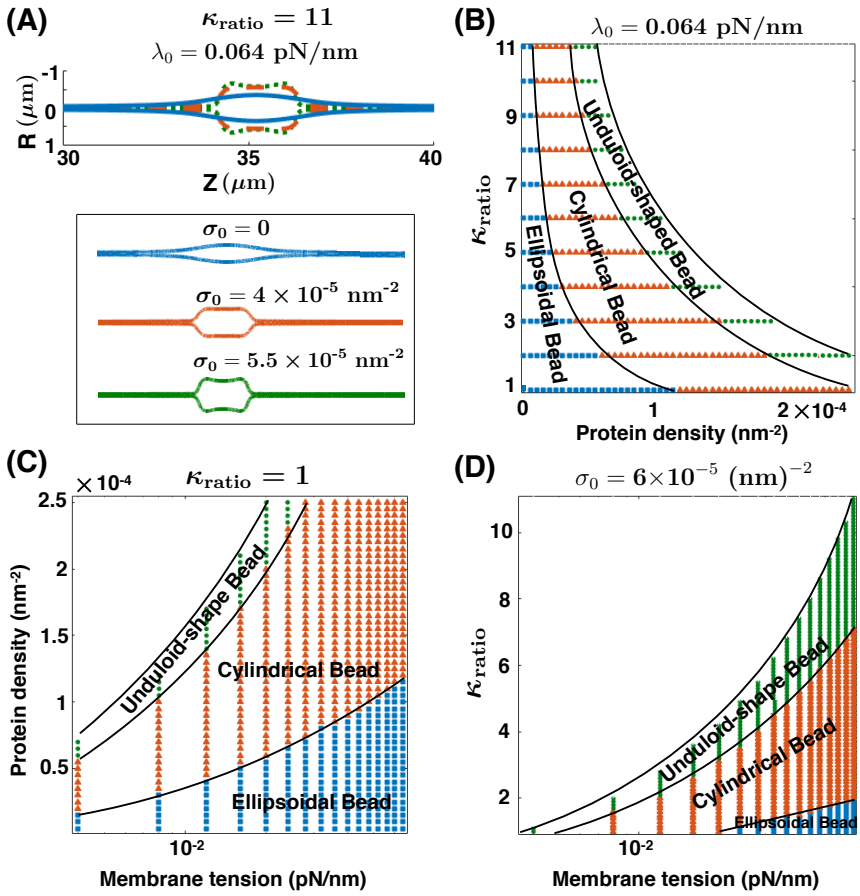

Figure 4: Bead morphology depends on the proteins density (σ_0), the bending rigidity ratio of the protein-enriched domain compared to the lipid membrane ($\kappa_{\rm ratio}$), and the edge membrane tension λ_0. (A) Three different possible shapes of a bead-like structure due to the presence of a rigid protein domain ($\kappa_{\rm ratio} = 11$); (*i*) An ellipsoidal bead (red) at low protein density, (*ii*) a cylindrical bead (blue) at average protein density, and (*iii*) an unduloid-shaped bead (green) at high protein density. (B) The phase diagram for bending rigidity ratio versus the number of the proteins per unit area, $\lambda_0 = 0.064\,\mathrm{pN/nm}$. The three different domains can be distinguished by the dominant length scale: (*i*) ellipsoidal beads when $\mathrm{L}_\sigma \gg \mathrm{L}_\mathrm{k}$, (*ii*) cylindrical beads when $\mathrm{L}_\sigma \sim \mathrm{L}_\mathrm{k}$, and (*iii*) unduloid-shaped beads when $\mathrm{L}_\mathrm{k} \gg \mathrm{L}_\sigma$. (C) The protein density versus the edge membrane tension λ_0 phase diagram for $\kappa_{\rm ratio} = 1$. (D) The bending rigidity ratio versus the edge membrane tension λ_0 phase diagram for $\sigma_0 = 6 \times 10^{-6}\ \mathrm{nm}^{-2}$. The colors in panels (C) and (D) represent same bead shapes as panel (B).

decreasing the area between the heterogeneity, there is a smooth transition from two beads connected by a string to a single bead (Fig. 5B, C). This suggests that at close distances, the energy minimum of the nanotube is attained for a single large bead rather than for two beads connected by a string. We also observe the smooth transition in number of beads is accompanied by the shape transition from an unduloid-shaped bead to a large ellipsoidal bead (Fig. 5C).

However, when we varied the area separation between the beads for a range of protein densities, we found a sharp transition from two beads to one bead accompanied by a snap-through instability (Fig. 5C,D,E). For small protein densities, when the area between the two beads is decreased, the nanotube appears to have one large bead, while the transition from two beads to one bead is continuous indicating that there is no energy barrier to go from one state to another (Fig. 5D, E, dashed, black line). However, as the protein density increases, we found the emergence of a snap-through instability for small separation areas (Fig. 5E) corresponding to bead shapes that show a distinct transition from two ellipsoids to a flower-shaped bead to a large ellipsoidal bead (Fig. 5E, green dashed line, F). This means that the landscape between two beads and one bead at high protein densities is

governed by a large energy barrier. And finally, when we repeated these calculations for a rigid protein domain such as $\kappa_{\text{ratio}} = 4$ (Fig. 5 G,H,I), we found that the area and protein density still govern the energy and stability landscape but the transition point – where the snap-through instability occurs – is shifted towards lower protein densities, with no change in bead shapes (Fig. 5G, H, I). Thus, protein-mediated beads along nanotubes potentially tend to be stable because any fusion event of two beads may often be accompanied by energy barriers and non-trivial shape transitions. This energy barrier corresponds to the length scale of domain separation being one order of magnitude larger than the length scale of the heterogeneity (see Fig. S10).

Discussion

Tunneling nanotubes, membranous projections between cells, have been identified as cellular transport highways [7–9]. Much of the biophysics associated with these dynamic structures are only now beginning to be explored but it is becoming increasingly clear that the cellular membrane and membrane-protein interactions play a critical role in maintaining these cellular highways [24, 27, 70, 75, 76]. In this study, we used systems biophysics to explore the energy landscape of nanotube formation and how heterogeneity in the membrane either due to material properties or protein aggregation affects these structures. Our results can be summarized as – membrane heterogeneity due to either membrane rigidity (Fig. 2) or protein-induced spontaneous curvature can result in the formation of bead-like structures along a nanotube (Fig. 3). Additionally, the interaction between these two modes of heterogeneity can lead to the formation of beads with distinct shapes while the transitions between these shapes from ellipsoidal to cylindrical to unduloid-shaped beads are consequences of competing length scales in the system (Fig. 4). Finally, the length scale competition induced by these effects coupled with the length scale between two regions of heterogeneity also governs the stability landscape of multiple beads (Fig .5). Although a similar interplay between adhesion and bending energy has been explored in shaping the plasma membrane and the shape of integrin adhesions, [77, 78], the shaping of membrane nanotubes resulting from the interplay between membrane heterogeneity due to a spatially varying membrane rigidity and protein-induced spontaneous curvature had not been previously been explored.

Our simulations allow us to make the following experimentally testable predictions. First, tension at the edge of the nanotube not only governs the nanotube radius but also its response to heterogeneity. Therefore, manipulating cell tension and evaluating how it affects the morphology of the nanotube will provide information on how tensional homeostasis of cells affects the membrane nanotubes. Additionally, we found that there is an energy barrier that governs the stability landscape of the transition from two beads to one bead. This energy barrier, governed by a snap-through instability suggests that the fusion of two beads depends on the membrane composition and its material properties such that under high protein density or high rigidity conditions, there is a large crossover energy for fusion. These predictions can be extend to multiple beads as well.

Although our model has provided some fundamental insights into the role of membrane composition in nanotube morphology, we have made simplifying assumptions that may need to be revisited as more experimental evidence is gathered regarding these structures. Additionally, the dynamics of membrane-protein diffusion and what could be the underlying mechanisms that govern protein aggregation along the nanotube as suggeste addressed by our model and are not yet fully understood. While there is evidence for strong curvature-mediated feedback for protein aggregation [56], it is possible that proteins in the lumen of the nanotube coupled with biochemical signaling can lead to the formation of protein microdomains. For exmaple, it is known that phase separation between two main components of the membrane – clusters of sphingolipids and cholesterol molecules – can result in formation of lipid rafts [67, 79]. Second, the role of the cytoskeleton (actin and microtubule filaments) and motor protein transport along the nanotube is known to be important [7, 8, 80] but a correlation with the beading morphology is yet to be established. And finally, the role of active transport versus flow of cytosolic components in governing the stability of these nanotubes is not captured by our model and remains an active focus of our research and modeling efforts. Despite our simplifying assumptions, our model provides insight into the morphological complexity of membrane nanotubes.

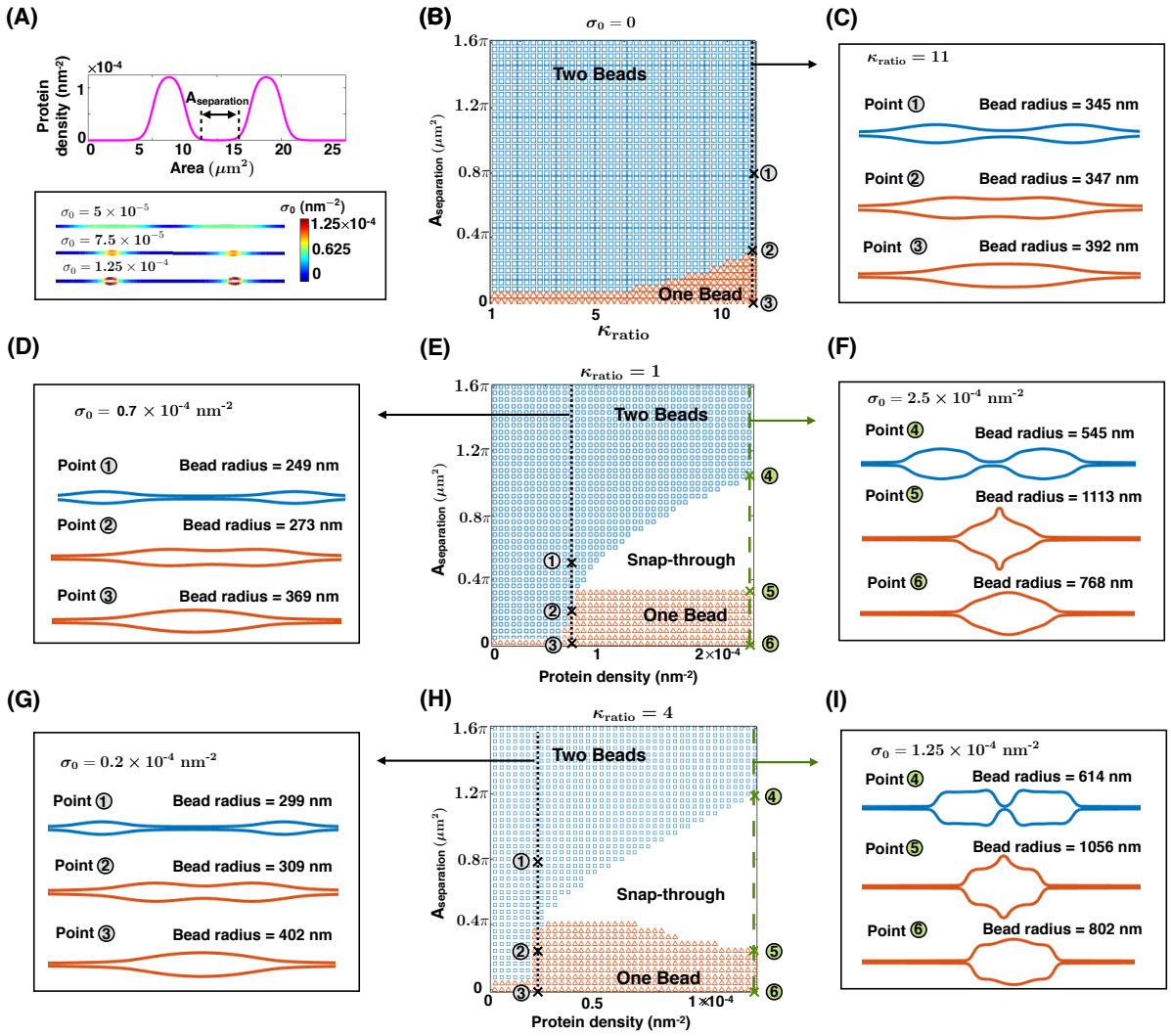

Figure 5: Multiple beads along a nanotube. (A, top) Protein density distribution with two domains of protein accumulation. The area of each protein-enriched domain is $A_{\text{protein}} = 1.6\pi\ \mu\text{m}^2$ and the domains are far from each other $A_{\text{separation}} = 1.6\pi\ \mu\text{m}^2$. The number of proteins within each domain increases by the same amount. (A, bottom) Two beads form corresponding to each protein-enriched domain, $\lambda_0 = 0.064\ \text{pN/nm}$. (B) The area separation between two beads versus the bending rigidity ratio phase diagram, $\sigma_0 = 0$. There are two possible shapes, (*i*) two separated beads denoted with color blue, and (*ii*) one single bead marked by color red. The transition from two to one bead is smooth everywhere in this parameter space. (C) The smooth membrane shape transition from two beads to one bead with decreasing area separation for $\kappa_{\text{ratio}} = 11$ and membrane profiles for points marked in panel (B). (D) Membrane profiles for the black dashed lines in panel (E) show the smooth evolution of membrane shape from two beads to one bead at $\sigma_0 = 0.7 \times 10^{-4}\ \text{nm}^{-2}$ for $\kappa_{\text{ratio}} = 1$ and increasing $A_{\text{separation}}$. (E) Phase diagram for the area separation between two beads versus the protein density at $\kappa_{\text{ratio}} = 1$. The colors represent same morphologies as panel (B). Smooth transition from two beads to one bead at low protein density and a snap-through instability in the transition from two beads to one bead for large protein densities are observed. (F) Membrane profiles show the snap-through transition from two kissing beads to one large bead at $\sigma_0 = 2.5 \times 10^{-4}\ \text{nm}^{-2}$ for the green dashed line in panel (E). (G) Membrane profiles for the black dashed lines in panel (H) show the smooth evolution of membrane shape from two beads to one bead at $\sigma_0 = 0.2 \times 10^{-4}\ \text{nm}^{-2}$ for $\kappa_{\text{ratio}} = 4$ and increasing $A_{\text{separation}}$. (H) Phase diagram for the area separation between two beads versus the protein density at $\kappa_{\text{ratio}} = 4$. The colors represent same morphologies as panel (B). Smooth transition from two beads to one bead at low protein density and a snap-through instability in the transition from two beads to one bead for large protein densities are observed. (I) Membrane profiles show the snap-through transition from two kissing beads to one large bead at $\sigma_0 = 1.25 \times 10^{-4}\ \text{nm}^{-2}$ for the green dashed line in panel (H).

Acknowledgment This work was supported by ARO W911NF-16-1-0411 grants to P.R. H.A. was supported by a fellowship from the Visible Molecular Cell Consortium (VMCC), a program between UCSD and the Scripps Research Institute. B.O. was supported by NIH R01GM111938. The authors would also like to thank Dr. Morgan Chabanon for his help on improving the manuscript.

References

[1] W. J. Lucas, B. Ding, and C. Schoot, "Plasmodesmata and the supracellular nature of plants," *New Phytol.*, vol. 125, no. 3, pp. 435–476, 1993.

[2] W. J. Lucas, S. Bouche-Pillon, D. P. Jackson, L. Nguyen, L. Baker, B. Ding, and S. Hake, "Selective trafficking of knotted1 homeodomain protein and its mrna through plasmodesmata," *Science*, vol. 270, no. 5244, pp. 1980–1983, 1995.

[3] S. Maeda and T. Tsukihara, "Structure of the gap junction channel and its implications for its biological functions," *Cell. Mol. Life Sci.*, vol. 68, no. 7, pp. 1115–1129, 2011.

[4] B. Alberts, *Molecular biology of the cell*. Garland science, 2017.

[5] A. Martin and G. Ringham, "Synaptic transfer at a vertebrate central nervous system synapse.," *J. Physiol.*, vol. 251, no. 2, pp. 409–426, 1975.

[6] A. B. Singh and R. C. Harris, "Autocrine, paracrine and juxtacrine signaling by EGFR ligands," *Cell. Signal.*, vol. 17, no. 10, pp. 1183–1193, 2005.

[7] A. Rustom, R. Saffrich, I. Markovic, P. Walther, and H.-H. Gerdes, "Nanotubular highways for intercellular organelle transport," *Sci.*, vol. 303, no. 5660, pp. 1007–1010, 2004.

[8] D. M. Davis and S. Sowinski, "Membrane nanotubes: dynamic long-distance connections between animal cells," *Nat. Rev. Mol. Cell. Biol.*, vol. 9, no. 6, p. 431, 2008.

[9] L. Marzo, K. Gousset, and C. Zurzolo, "Multifaceted roles of tunneling nanotubes in intercellular communication," *Fron. Physiol*, vol. 3, 2012.

[10] G. Haimovich, C. M. Ecker, M. C. Dunagin, E. Eggan, A. Raj, J. E. Gerst, and R. H. Singer, "Intercellular mrna trafficking via membrane nanotube-like extensions in mammalian cells," *Proc. Natl. Acad. Sci.*, vol. 114, no. 46, pp. E9873–E9882, 2017.

[11] H.-H. Gerdes and R. N. Carvalho, "Intercellular transfer mediated by tunneling nanotubes," *Curr. Opin. Cell. Biol*, vol. 20, no. 4, pp. 470–475, 2008.

[12] B. Onfelt, S. Nedvetzki, K. Yanagi, and D. M. Davis, "Cutting edge: Membrane nanotubes connect immune cells," *J. Immunol*, vol. 173, no. 3, pp. 1511–1513, 2004.

[13] S. Sowinski, C. Jolly, O. Berninghausen, M. A. Purbhoo, A. Chauveau, K. Kohler, S. Oddos, P. Eissmann, F. M. Brodsky, C. Hopkins, *et al.*, "Membrane nanotubes physically connect t cells over long distances presenting a novel route for hiv-1 transmission," *Nat. Cell. Biol*, vol. 10, no. 2, p. 211, 2008.

[14] T. Bhatia, J. Agudo-Canalejo, R. Dimova, and R. Lipowsky, "Membrane nanotubes increase the robustness of giant vesicles," *ACS Nano*, vol. 12, no. 5, pp. 4478–4485, 2018.

[15] R. W. Davenport, P. Dou, V. Rehder, and S. Kater, "A sensory role for neuronal growth cone filopodia," *Nature*, vol. 361, no. 6414, p. 721, 1993.

[16] S. L. Gupton and F. B. Gertler, "Filopodia: the fingers that do the walking," *Sci. Signal.*, vol. 2007, no. 400, p. re5, 2007.

[17] N. S. Parkar, B. S. Akpa, L. C. Nitsche, L. E. Wedgewood, A. T. Place, M. S. Sverdlov, O. Chaga, and R. D. Minshall, "Vesicle formation and endocytosis: function, machinery, mechanisms, and modeling," *Antioxid. Redox Signal.*, vol. 11, no. 6, pp. 1301–1312, 2009.

[18] L. Caneparo, P. Pantazis, W. Dempsey, and S. E. Fraser, "Intercellular bridges in vertebrate gastrulation," *PLoS One*, vol. 6, no. 5, p. e20230, 2011.

[19] X. Wang, N. V. Bukoreshtliev, and H.-H. Gerdes, "Developing neurons form transient nanotubes facilitating electrical coupling and calcium signaling with distant astrocytes," *PloS one*, vol. 7, no. 10, p. e47429, 2012.

[20] D. L. Tanelian and V. S. Markin, "Biophysical and functional consequences of receptor-mediated nerve fiber transformation," *Biophys. J.*, vol. 72, no. 3, pp. 1092–1108, 1997.

[21] E. Lou, "Intercellular conduits in tumors: The new social network," *Trends in cancer*, vol. 2, no. 1, pp. 3–5, 2016.

[22] H.-H. Gerdes, A. Rustom, and X. Wang, "Tunneling nanotubes, an emerging intercellular communication route in development," *Mech. Dev.*, vol. 130, no. 6-8, pp. 381–387, 2013.

[23] Y. Liu, J. Agudo-Canalejo, A. Grafmuller, R. Dimova, and R. Lipowsky, "Patterns of flexible nanotubes formed by liquid-ordered and liquid-disordered membranes," *ACS Nano*, vol. 10, no. 1, pp. 463–474, 2015.

[24] A. Iglivc, B. Babnik, U. Gimsa, and V. Kralj-Iglivc, "On the role of membrane anisotropy in the beading transition of undulated tubular membrane structures," *J. Phys. A*, vol. 38, no. 40, p. 8527, 2005.

[25] A. H. Bahrami and G. Hummer, "Formation and stability of lipid membrane nanotubes," *ACS Nano*, vol. 11, no. 9, pp. 9558–9565, 2017.

[26] H. Alimohamadi, B. Ovryn, and P. Rangamani, "Protein-mediated beads-on-a-string structure formation along membrane nanotubes in live cells," *Biophys. J.*, vol. 114, no. 3, p. 392a, 2018.

[27] H. Jiang, B. P. English, R. B. Hazan, P. Wu, and B. Ovryn, "Tracking surface glycans on live cancer cells with single-molecule sensitivity," *Angew. Chem.*, vol. 54, no. 6, pp. 1765–1769, 2015.

[28] U. Jelerčič and N. S. Gov, "Pearling instability of membrane tubes driven by curved proteins and actin polymerization," *Phys. Biol.*, vol. 12, no. 6, p. 066022, 2015.

[29] B. J. Allen, S. D. Rogers, J. R. Ghilardi, P. M. Menning, M. A. Kuskowski, A. I. Basbaum, D. A. Simone, and P. W. Mantyh, "Noxious cutaneous thermal stimuli induce a graded release of endogenous substance p in the spinal cord: Imaging peptide actionin vivo," *J. Neurosci.*, vol. 17, no. 15, pp. 5921–5927, 1997.

[30] S. C. Watkins and R. D. Salter, "Functional connectivity between immune cells mediated by tunneling nanotubules," *Immunity*, vol. 23, no. 3, pp. 309–318, 2005.

[31] S. Ochs, R. Pourmand, R. A. Jersild, and R. N. Friedman, "The origin and nature of beading: a reversible transformation of the shape of nerve fibers," *Prog. Neurobiol.*, vol. 52, no. 5, pp. 391–426, 1997.

[32] D. Kilinc, G. Gallo, and K. A. Barbee, "Mechanical membrane injury induces axonal beading through localized activation of calpain," *Exp. Neurol.*, vol. 219, no. 2, pp. 553–561, 2009.

[33] V. S. Markin, D. L. Tanelian, R. A. Jersild Jr, and S. Ochs, "Biomechanics of stretch-induced beading," *Biophys. J.*, vol. 76, no. 5, pp. 2852–2860, 1999.

[34] R. Bar-Ziv and E. Moses, "Instability and" pearling" states produced in tubular membranes by competition of curvature and tension," *Phys. Rev. Lett.*, vol. 73, no. 10, p. 1392, 1994.

[35] T. R. Powers and R. E. Goldstein, "Pearling and pinching: propagation of rayleigh instabilities," *Phys. Rev. Lett.*, vol. 78, no. 13, p. 2555, 1997.

[36] G. Boedec, M. Jaeger, and M. Leonetti, "Pearling instability of a cylindrical vesicle," *J. Fluid Mech.*, vol. 743, pp. 262–279, 2014.

[37] R. Lipowsky, "Spontaneous tubulation of membranes and vesicles reveals membrane tension generated by spontaneous curvature," *Faraday Discuss.*, vol. 161, pp. 305–331, 2013.

[38] M. E. A. Faris, D. Lacoste, J. Pécréaux, J.-F. Joanny, J. Prost, and P. Bassereau, "Membrane tension lowering induced by protein activity," *Phys. Rev. Lett.*, vol. 102, no. 3, p. 038102, 2009.

[39] P. Rangamani, K. K. Mandadap, and G. Oster, "Protein-induced membrane curvature alters local membrane tension," *Biophys. J.*, vol. 107, no. 3, pp. 751–762, 2014.

[40] J.-B. Manneville, P. Bassereau, S. Ramaswamy, and J. Prost, "Active membrane fluctuations studied by micropipet aspiration," *Phys. Rev. Lett.*, vol. 64, no. 2, p. 021908, 2001.

[41] Z. Shi, Z. T. Graber, T. Baumgart, H. A. Stone, and A. E. Cohen, "Cell membranes resist flow," *bioRxiv*, p. 290643, 2018.

[42] M. Chabanon and P. Rangamani, "Gaussian curvature directs the distribution of spontaneous curvature on bilayer membrane necks," *Soft Matter*, 2018.

[43] A. Agrawal and D. J. Steigmann, "A model for surface diffusion of trans-membrane proteins on lipid bilayers," *ZAMP*, vol. 62, no. 3, pp. 549–563, 2011.

[44] T. Belay, C. I. Kim, and P. Schiavone, "Bud formation of lipid membranes in response to the surface diffusion of transmembrane proteins and line tension," *Mathematics and Mechanics of Solids*, p. 1081286516657684, 2016.

[45] W. Helfrich, "Elastic properties of lipid bilayers: theory and possible experiments," *Zeitschrift fur Naturforschung C*, vol. 28, no. 11-12, pp. 693–703, 1973.

[46] J. E. Hassinger, G. Oster, D. G. Drubin, and P. Rangamani, "Design principles for robust vesiculation in clathrin-mediated endocytosis," *Proc. Natl. Acad. Sci.*, vol. 114, no. 7, pp. E1118–E1127, 2017.

[47] S. E. Miller, S. Mathiasen, N. A. Bright, F. Pierre, B. T. Kelly, N. Kladt, A. Schauss, C. J. Merrifield, D. Stamou, S. Honing, *et al.*, "Calm regulates clathrin-coated vesicle size and maturation by directly sensing and driving membrane curvature," *Dev. Cell*, vol. 33, no. 2, pp. 163–175, 2015.

[48] D. Steigmann, "Fluid films with curvature elasticity," *Arch. Ration. Mech. Anal.*, vol. 150, no. 2, pp. 127–152, 1999.

[49] D. Steigmann, E. Baesu, R. E. Rudd, J. Belak, and M. McElfresh, "On the variational theory of cell-membrane equilibria," *IFB*, vol. 5, no. 4, pp. 357–366, 2003.

[50] W. Rawicz, K. Olbrich, T. McIntosh, D. Needham, and E. Evans, "Effect of chain length and unsaturation on elasticity of lipid bilayers," *Biophys. J.*, vol. 79, no. 1, pp. 328–339, 2000.

[51] P. Rangamani, A. Agrawal, K. K. Mandadapu, G. Oster, and D. J. Steigmann, "Interaction between surface shape and intra-surface viscous flow on lipid membranes," *Biomech. Model. Mechanobiol.*, pp. 1–13, 2013.

[52] J. Jenkins, "Static equilibrium configurations of a model red blood cell," *J. Math. Biol.*, vol. 4, no. 2, pp. 149–169, 1977.

[53] D. J. Steigmann, "Mechanics and physics of lipid bilayers," in *The Role of Mechanics in the Study of Lipid Bilayers*, pp. 1–61, Springer, 2018.

[54] A. Callan-Jones, M. Durand, and J.-B. Fournier, "Hydrodynamics of bilayer membranes with diffusing transmembrane proteins," *Soft matter*, vol. 12, no. 6, pp. 1791–1800, 2016.

[55] P. Wiggins and R. Phillips, "Membrane-protein interactions in mechanosensitive channels," *Biophys. J.*, vol. 88, no. 2, pp. 880–902, 2005.

[56] N. Gov, "Guided by curvature: shaping cells by coupling curved membrane proteins and cytoskeletal forces," *Phil. Trans. R. Soc. B*, vol. 373, no. 1747, p. 20170115, 2018.

[57] M. Karlsson, M. Davidson, R. Karlsson, A. Karlsson, J. Bergenholtz, Z. Konkoli, A. Jesorka, T. Lobovkina, J. Hurtig, M. Voinova, *et al.*, "Biomimetic nanoscale reactors and networks," *Annu. Rev. Phys. Chem.*, vol. 55, pp. 613–649, 2004.

[58] B. Bauer, M. Davidson, and O. Orwar, "Direct reconstitution of plasma membrane lipids and proteins in nanotube- vesicle networks," *Langmuir*, vol. 22, no. 22, pp. 9329–9332, 2006.

[59] L. Landau, "Em lifshitz fluid mechanics," *Course of Theoretical Physics*, vol. 6, 1959.

[60] A. Veksler and N. S. Gov, "Phase transitions of the coupled membrane-cytoskeleton modify cellular shape," *Biophys. J.*, vol. 93, no. 11, pp. 3798–3810, 2007.

[61] N. Walani, J. Torres, and A. Agrawal, "Endocytic proteins drive vesicle growth via instability in high membrane tension environment," *Proc. Natl. Acad. Sci.*, vol. 112, no. 12, pp. E1423–E1432, 2015.

[62] A. Agrawal and D. J. Steigmann, "Boundary-value problems in the theory of lipid membranes," *Continuum. Mech. Therm.*, vol. 21, no. 1, pp. 57–82, 2009.

[63] J. C. Stachowiak, F. M. Brodsky, and E. A. Miller, "A cost-benefit analysis of the physical mechanisms of membrane curvature," *Nat. Cell. Biol*, vol. 15, no. 9, pp. 1019–1027, 2013.

[64] J. Dai, M. P. Sheetz, X. Wan, and C. E. Morris, "Membrane tension in swelling and shrinking molluscan neurons," *Journal of Neuroscience*, vol. 18, no. 17, pp. 6681–6692, 1998.

[65] R. Dimova, "Recent developments in the field of bending rigidity measurements on membranes," *Advances in colloid and interface science*, vol. 208, pp. 225–234, 2014.

[66] M. Lokar, D. Kabaso, N. Resnik, K. Sepčić, V. Kralj-Iglič, P. Veranič, R. Zorec, and A. Iglič, "The role of cholesterol-sphingomyelin membrane nanodomains in the stability of intercellular membrane nanotubes," *Int. J. Nanomed.*, vol. 7, p. 1891, 2012.

[67] A. J. Laude and I. A. Prior, "Plasma membrane microdomains: organization, function and trafficking," *Mol. Membr. Biol.*, vol. 21, no. 3, pp. 193–205, 2004.

[68] S. Dmitrieff and F. Nedelec, "Membrane mechanics of endocytosis in cells with turgor," *PLOS Comput. Biol.*, vol. 11, no. 10, p. e1004538, 2015.

[69] S. Ramadurai, A. Holt, V. Krasnikov, G. van den Bogaart, J. A. Killian, and B. Poolman, "Lateral diffusion of membrane proteins," *J. Am. Chem. Soc.*, vol. 131, no. 35, pp. 12650–12656, 2009.

[70] M. E. Kurczy, L. J. Mellander, N. Najafinobar, and A.-S. Cans, "Composition based strategies for controlling radii in lipid nanotubes," *Plos one*, vol. 9, no. 1, p. e81293, 2014.

[71] M. Yanagisawa, M. Imai, and T. Taniguchi, "Shape deformation of ternary vesicles coupled with phase separation," *Phys. Rev. Lett.*, vol. 100, no. 14, p. 148102, 2008.

[72] D. Brown and E. London, "Functions of lipid rafts in biological membranes," *Annu. Rev. Cell Dev. Biol.*, vol. 14, no. 1, pp. 111–136, 1998.

[73] T. Baumgart, S. Das, W. Webb, and J. Jenkins, "Membrane elasticity in giant vesicles with fluid phase coexistence," *Biophys. J.*, vol. 89, no. 2, pp. 1067–1080, 2005.

[74] I. Derenyi, F. Julicher, and J. Prost, "Formation and interaction of membrane tubes," *Phys. Rev. Lett.*, vol. 88, no. 23, p. 238101, 2002.

[75] Y. Li, R. Lipowsky, and R. Dimova, "Membrane nanotubes induced by aqueous phase separation and stabilized by spontaneous curvature," *Proc. Natl. Acad. Sci.*, vol. 108, no. 12, pp. 4731–4736, 2011.

[76] H. Alimohamadi, R. Vasan, J. Hassinger, J. Stachowiak, and P. Rangamani, "The role of traction in membrane curvature generation," *Biophys. J.*, vol. 114, no. 3, p. 600a, 2018.

[77] E. Atilgan and B. Ovryn, "Nucleation and growth of integrin adhesions," *Biophys. J.*, vol. 96, no. 9, pp. 3555–3572, 2009.

[78] T. R. Weikl, J. Hu, G.-K. Xu, and R. Lipowsky, "Binding equilibrium and kinetics of membrane-anchored receptors and ligands in cell adhesion: Insights from computational model systems and theory," *Cell. Adhes. Migr*, vol. 10, no. 5, pp. 576–589, 2016.

[79] F. R. Maxfield, "Plasma membrane microdomains," *Curr. Opin. Cell. Biol.*, vol. 14, no. 4, pp. 483–487, 2002.

[80] E. Delage, D. C. Cervantes, E. Penard, C. Schmitt, S. Syan, A. Disanza, G. Scita, and C. Zurzolo, "Differential identity of filopodia and tunneling nanotubes revealed by the opposite functions of actin regulatory complexes," *Sci. Rep.*, vol. 6, p. 39632, 2016.

Supplementary material for "Protein aggregation and membrane bending govern nanotube morphology"

H. Alimohamadi[1], B. Ovryn[2] and P. Rangamani[*1]

[1]Department of Mechanical and Aerospace Engineering, University of California San Diego, CA 92093, USA
[2]Department of Electrical and Computer Engineering Colorado State University, CO 80523, USA

July 18, 2018

Contents

1 Model Development **2**
1.1 Equations of motion 2
1.2 Helfrich energy and mechanical equilibrium 3
1.3 Equations of motion in axisymmetric coordinates 4
1.3.1 Numerical implementation 6

2 Tables **7**
2.1 Table of Notation 7
2.2 Table of parameters 9

3 Supplementary Figures **10**

[*]prangamani@ucsd.edu

1 Model Development

1.1 Equations of motion

In this section, we present a brief derivation of the generalized equations of motion for biological membranes under the assumptions stated in the main text. We then restrict the equations to axisymmetric coordinates and solve them in a prescribed membrane area domain. Details of all derivations can be found in [1–3].
The local force balance in the absence of inertia for any material point on the membrane is

$$\mathbf{\Gamma}^{\xi}_{;\xi} + p\mathbf{n} = 0, \tag{S1}$$

where $(_{;\xi})$ is the surface divergence, $\mathbf{\Gamma}^{\xi}$ is the stress vector, p is the pressure difference between the inside and outside of the volume bounded by the membrane, and $\mathbf{n}$ is the unit vector normal to the membrane. The surface divergence in Eq. (S1) can be rewritten as [1]

$$\mathbf{\Gamma}^{\xi}_{;\xi} = (\sqrt{a})^{-1}(\sqrt{a}\mathbf{\Gamma}^{\xi})_{,\xi}, \tag{S2}$$

where a is the determinant of the first fundamental form metric $a_{\xi\eta}$. The stress vector in Eq. (S1) can be decomposed into normal and tangential components as

$$\mathbf{\Gamma}^{\xi} = \boldsymbol{T}^{\xi} + S^{\xi}\mathbf{n}. \tag{S3}$$

For elastic surfaces for which the energy density per unit mass $F(a_{\xi\eta},\, b_{\xi\eta})$ responds to the first and second fundamental forms, the normal and tangential components of the stress vector in Eq. (S3) can be expressed as [1, 4]

$$\mathbf{T}^{\xi} = T^{\xi\eta}\mathbf{a}_{\eta} \quad \text{with} \quad T^{\xi\eta} = \Gamma^{\xi\eta} + b^{\eta}_{\mu}M^{\mu\xi}, \quad \text{and} \quad S^{\xi} = -M^{\xi\eta}_{;\eta}, \tag{S4}$$

where

$$\Gamma^{\xi\eta} = \rho\left(\frac{\partial F(\rho, H, K; x^{\xi})}{\partial a_{\xi\eta}} + \frac{\partial F(\rho, H, K; x^{\xi})}{\partial a_{\eta\xi}}\right), \quad M^{\xi\eta} = \frac{\rho}{2}\left(\frac{\partial F(\rho, H, K; x^{\xi})}{\partial b_{\xi\eta}} + \frac{\partial F(\rho, H, K; x^{\xi})}{\partial b_{\eta\xi}}\right). \tag{S5}$$

Here, ρ is the surface mass density, and H and K are the mean and Gaussian curvatures given by

$$H = \frac{1}{2}a^{\xi\eta}b_{\xi\eta}, \quad K = \frac{1}{2}\varepsilon^{\xi\eta}\varepsilon^{\lambda\mu}b_{\xi\lambda}b_{\eta\mu}. \tag{S6}$$

Here $(a^{\xi\eta}) = (a_{\xi\eta})$ is the dual metric and $\varepsilon^{\xi\eta}$ is the permutation tensor defined by $\varepsilon^{12} = -\varepsilon^{21} = 1/\sqrt{a}, \varepsilon^{11} = \varepsilon^{22} = 0$.

In the case of area incompressibility ($J = 1$), the general form of free energy density per unit mass can be rewritten as

$$F(\rho, H, K; x^{\xi}) = \tilde{F}(H, K; x^{\xi}) - \frac{\gamma(x^{\xi}, t)}{\rho}, \tag{S7}$$

where $\gamma(x^{\xi}, t)$ is a Lagrange multiplier field required to impose invariance of ρ on the whole of the surface (see [1] for full derivation). Substituting $W = \rho\tilde{F}$ into Eq. (S7) we get

$$\Gamma^{\xi\eta} = (\lambda + W)a^{\xi\eta} - (2HW_H + 2\kappa W_K)a^{\xi\eta} + W_H\tilde{b}^{\xi\eta}, \tag{S8}$$

$$M^{\xi\eta} = \frac{1}{2}W_H a^{\xi\eta} + W_K\tilde{b}^{\xi\eta}, \tag{S9}$$

where $\tilde{b^{\xi\eta}}$ is the co-factor of the curvature tensor, and $\lambda = -(\gamma + W)$ can be interpreted as the membrane tension [5].

Combining Eqs. (S9), (S4), and (S3) with Eq. (S1) gives the equation of motion in normal and tangential directions as

$$\text{Normal:} \quad p = \Delta\frac{1}{2}W_H + (W_K)_{;\xi\eta}\tilde{b}^{\xi\eta} + W_H(2H^2 - K) + 2H(KW_K - W) - 2\lambda H, \tag{S10}$$

and

$$\text{Tangential:} \quad N^{\eta\xi}_{;\xi} - S^{\xi}b^{\eta}_{\xi} = -(\gamma_{,\xi} + W_K k_{,\xi} + W_H H_{,\xi})a^{\eta\xi} = (\frac{\partial W}{\partial x^{\xi}}|_{\text{exp}} + \lambda_{,\xi})a^{\eta\xi} = 0. \tag{S11}$$

Here $\Delta(\cdot)$ is the surface Laplacian, and $()_{|\text{exp}}$ denotes the explicit derivative respect to coordinate θ^{ξ}.

1.2 Helfrich energy and mechanical equilibrium

For the local energy density of a lipid bilayer membrane, we use an augmented version of the Helfrich energy accounting for an energy associated with the local protein density ($\sigma(\theta^{\xi})$) [3, 6–8]

$$W = (\alpha\sigma)^2 + \kappa(\theta^{\xi})(H - C(\sigma))^2 + \kappa_G(\theta^{\xi})K, \tag{S12}$$

where W is the local energy density, C is the induced spontaneous curvature due to lipid-protein interactions, κ is the bending modulus, and κ_G is the Gaussian modulus. In Eq. (S12), α is a positive constant representing derivative of the chemical potential with respect to the protein density at constant pressure and temperature [8]. It should be noted that Eq. (S12) is different from the standard Helfrich energy by a factor of 2. We take this net effect into consideration by choosing the value of the bending modulus to be twice that of the standard value of bending modulus typically used for lipid bilayers [9].

For low protein densities (dilute regime), the induced-spontaneous curvature $C(\sigma)$ in Eq. (S12) can be expressed in term of protein density as [6]

$$C(\sigma) = (\mu\varphi)\sigma, \tag{S13}$$

where φ is the angle between cone-shaped proteins meridian and the normal vector to the surface (**n**), and μ is a length-scale correction representing the lipid-protein specific moietic interaction (see Fig. 1) [10].

Substituting the modified version of Helfrich energy function (Eq. (S12)) and Eq. (S13) into the first functional normal variation of total energy (Eq. (S10)) gives the so-called "shape equation," [11]

$$\underbrace{\Delta\left[\kappa\left(H - (\mu\varphi)\sigma\right)\right] - (\kappa_G)_{;\xi\eta}\tilde{b}^{\xi\eta} + 2\kappa\left(H - (\mu\varphi)\sigma\right)\left(2H^2 - K\right) - 2\kappa H\left(H - (\mu\varphi)\sigma\right)^2}_{\text{Elastic effects}} - \underbrace{2H(\alpha\sigma)^2}_{\text{Protein density effect}} = \underbrace{(p + 2\lambda H)}_{\text{Capillary effect}}. \tag{S14}$$

A consequence of spatial variation of membrane properties and protein density is that λ is not homogeneous along the membrane [5, 12, 13]. Substituting Eq. (S12) into the balance of forces tangential to the membrane Eq. (S11) gives the spatial variation of membrane tension,

$$\underbrace{\nabla\lambda}_{\substack{\text{Gradient of}\\ \text{surface tension}}} = \underbrace{2[\kappa\mu\varphi(H-(\mu\varphi)\sigma)-\alpha(\alpha\sigma)]\frac{\partial\sigma}{\partial\theta^{\xi}}}_{\text{Protein density variation}} - \underbrace{\frac{\partial\kappa}{\partial\theta^{\xi}}(H-(\mu\varphi)\sigma)^2}_{\substack{\text{Bending modulus-}\\ \text{induced variation}}} - \underbrace{\frac{\partial\kappa_G}{\partial\theta^{\xi}}K}_{\substack{\text{Gaussian modulus-}\\ \text{induced variation}}}, \tag{S15}$$

where ∇ is the partial derivative with respect to the coordinate (θ^{ξ}).

1.3 Equations of motion in axisymmetric coordinates

We define a surface of revolution (Fig. 1C) by

$$\mathbf{r}(s,\theta) = R(s)\mathbf{e}_r(\theta) + Z(s)\mathbf{k}, \tag{S16}$$

where s is the arc length along the curve, R(s) is the radius from the axis of rotation, Z(s) is the height from the base plane and $(\mathbf{e}_r, \mathbf{e}_\theta, \mathbf{k})$ form the basis coordinate. Defining ψ as the angle made by the tangent with respect to the vertical gives

$$R'(s) = \cos(\psi), \quad Z'(s) = \sin(\psi), \tag{S17}$$

satisfying the identity $(R')^2 + (Z')^2 = 1$, where $(')$ is the partial derivative with respect to the arc length. Using this, we can define the normal and tangent vectors to the surface as

$$\mathbf{n} = -\sin\psi\mathbf{e}_r(\theta) + \cos\psi\mathbf{k}, \quad \mathbf{a}_s = \cos\psi\mathbf{e}_r(\theta) + \sin\psi\mathbf{k}. \tag{S18}$$

Using this parameterization, we can now write the tangential (κ_ν) and transverse (κ_τ) curvatures as

$$\kappa_\nu = \psi', \quad \kappa_\tau = \frac{\sin\psi}{R}. \tag{S19}$$

The mean curvature (H) and Gaussian curvature (K) are obtained by summation and multiplication of the tangential and transverse curvatures

$$H = \frac{1}{2}(\kappa_\nu + \kappa_\tau) = \frac{1}{2}(\psi' + \frac{\sin\psi}{R}), \quad K = \kappa_\tau\kappa_\nu = \frac{\psi'\sin\psi}{R}. \tag{S20}$$

Finally, we define $L = \frac{1}{2\kappa}R(W_H)'$ such that we obtain a system of first- order differential equations with six unknowns R, Z, ψ, H, L, and λ [11, 13],

$$\begin{aligned}
&R' = \cos\psi, \quad Z' = \sin\psi, \quad R\psi' = 2RH - \sin\psi, \quad RH' = L + R\mu\varphi\sigma' - \frac{R\kappa'}{\kappa}(H-\mu\varphi\sigma),\\
&\frac{L'}{R} = \frac{p}{k} + 2H\left[(H-(\mu\varphi)\sigma)^2 + \frac{(\alpha\sigma)^2}{\kappa} + \frac{\lambda}{\kappa}\right] - 2\left(H-(\mu\varphi)\sigma\right)\left[H^2 + \left(H - \frac{\sin\psi}{R}\right)^2\right]\\
&\qquad - \frac{\kappa' L}{\kappa R} - \frac{\kappa_G''\sin(\psi)}{\kappa R} - \frac{\kappa_G'\cos(\psi)}{\kappa R}(2H - \frac{\sin(\psi)}{R}),\\
&\lambda' = 2\Big[\kappa\mu\varphi\left(H-\mu\varphi\sigma\right) - 2\alpha(\alpha\sigma)\Big]\sigma' - \kappa'(H-(\mu\varphi)\sigma)^2 - \kappa_G' K.
\end{aligned} \tag{S21}$$

In order to solve this system of equations (Eq. (S21)), we need to provide six boundary conditions. We consider an axisymmetric cylindrical membrane with (1) fixed radius at both boundaries, (2) $\psi = \pi/2$ at both ends to ensure

the edges remain vertical, (3) fixed height at one end and prescribed tension (λ_0) at the other end (see Fig. 1C). These boundary conditions can be summarized as follow,

$$\begin{aligned} R(0^+) = R_0, \quad \psi(0^+) = \frac{\pi}{2}, \quad z(0^+) = 0, \\ R(\mathrm{s_{max}}) = R_0, \quad \psi(\mathrm{s_{max}}) = \frac{\pi}{2}, \quad \lambda(\mathrm{s_{max}}) = \lambda_0. \end{aligned} \tag{S22}$$

One advantage of an asymmetric coordinate system is that the manifold area (A) can be expressed in term of arc length [13],

$$A(s) = 2\pi \int_0^s R(\eta) d\eta \quad \rightarrow \quad \frac{dA}{ds} = 2\pi R. \tag{S23}$$

Thus, Eq. (S23) allows us to convert the system of equations in Eq. (S21) that are in term of arc length to a system in terms of area. So, we can prescribe the total area of the membrane instead of arc length

$$\begin{aligned} 2\pi R\dot{R} = \cos\psi, \quad 2\pi R\dot{Z} = \sin\psi, \quad 2\pi R^2\dot{\psi} = 2RH - \sin\psi, \quad 2\pi R^2\dot{H} = L + 2\pi\mu\varphi R^2\dot{\sigma} - \frac{2\pi R^2\dot{\kappa}}{\kappa}(H - \mu\varphi\sigma), \\ 2\pi\dot{L} = \frac{p}{k} + 2H\left[(H-\mu\varphi\sigma)^2 + \frac{(\alpha\sigma)^2}{\kappa} + \frac{\lambda}{\kappa}\right] - 2\left(H - \mu\varphi\sigma\right)\left[H^2 + \left(H - \frac{\sin\psi}{R}\right)^2\right] \\ -2\pi\frac{\dot{\kappa}L}{\kappa} - 4\pi^2 r\frac{\ddot{\kappa}_G\sin(\psi)}{\kappa} - 2\pi\frac{\dot{\kappa}_G\cos(\psi)}{\kappa}(2H - \frac{\sin(\psi)}{R}), \\ 2\pi R\dot{\lambda} = 4\pi R\Big[\kappa\mu\varphi\left(H - \mu\varphi\sigma\right) - 2\alpha(\alpha\sigma)\Big]\dot{\sigma} - 2\pi R\dot{\kappa}(H - (\mu\varphi)\sigma)^2 - 2\pi R\dot{\kappa}_G K, \end{aligned} \tag{S24}$$

where ($\dot{}$) denotes the derivative with respect to the area. The boundary conditions Eq. (S22) remain unchanged, and the upper limit of the domain changes to $A_{\max}$ instead of $s_{\max}$.

To non-dimensionalize the system of equations (Eq. (S24)), we use two parameters, the radius of the initial cylindrical membrane (R_0), and lipid bilayer bending modulus (κ_{lipid}). Using these constants, we can define

$$\begin{aligned} \zeta = \frac{A}{2\pi R_0^2}, \quad y = \frac{Z}{R_0}, \quad x = \frac{R}{R_0}, \quad h = HR_0, \quad c = CR_0, \quad l = LR_0, \quad \tilde{\lambda} = \frac{\lambda R_0^2}{\kappa_{\text{lipid}}}, \quad G = KR_0^2 \\ \tilde{p} = \frac{pR_0^3}{\kappa_{\text{lipid}}}, \quad \tilde{\kappa}_G = \frac{\kappa_G}{\kappa_{\text{lipid}}}, \quad \tilde{\kappa} = \frac{\kappa}{\kappa_{\text{lipid}}}, \quad \tilde{\alpha} = \frac{\alpha}{R_0\sqrt{\kappa_{\text{lipid}}}}, \quad \tilde{\mu} = \frac{\mu}{R_0}, \quad \tilde{\sigma} = \frac{\sigma}{R_0^2}. \end{aligned} \tag{S25}$$

Rewriting Eq. (S24) in terms of the dimensionless variables in Eq. (S25), we get [13]

$$\begin{aligned} x\dot{x} = \cos\psi, \quad x\dot{y} = \sin\psi, \quad x^2\dot{\psi} = 2xh - \sin\psi, \quad x^2\dot{h} = l + x^2\dot{\tilde{\sigma}} - x^2\frac{\dot{\tilde{\kappa}}}{\tilde{\kappa}}(h - \tilde{\mu}\varphi\tilde{\sigma}), \\ \dot{l} = \frac{\tilde{p}}{\tilde{\kappa}} + 2h\left[(h - (\tilde{\mu}\varphi)\tilde{\sigma})^2 + \frac{(\tilde{\alpha}\tilde{\sigma})^2}{\tilde{\kappa}} + \frac{\tilde{\lambda}}{\tilde{\kappa}}\right] - 2\left(h - (\tilde{\mu}\varphi)\tilde{\sigma}\right)\left[h^2 + \left(h - \frac{\sin\psi}{x}\right)^2\right] \\ -\frac{\dot{\tilde{\kappa}}}{\tilde{\kappa}}l - x\frac{\ddot{\tilde{\kappa}}_G}{\tilde{\kappa}}\sin(\psi) - \frac{\dot{\tilde{\kappa}}_G}{\tilde{\kappa}}\cos(\psi)(2h - \frac{\sin(\psi)}{x}), \\ \dot{\tilde{\lambda}} = 2\Big[\tilde{\kappa}\tilde{\mu}\varphi\left(H - \tilde{\mu}\varphi\tilde{\sigma}\right) - 2\tilde{\alpha}(\tilde{\alpha}\tilde{\sigma})\Big]\dot{\sigma} - \dot{\tilde{\kappa}}(h - (\tilde{\mu}\varphi)\tilde{\sigma})^2 - \dot{\tilde{\kappa}}_G G, \end{aligned} \tag{S26}$$

and the boundary conditions in Eq. (S22) simplify to

$$x(0^+) = 1, \quad \psi(0^+) = \frac{\pi}{2}, \quad y(0^+) = 0,$$
$$x(\zeta_{\max}) = 1, \quad \psi(\zeta_{\max}) = \frac{\pi}{2}, \quad \tilde{\lambda}(\zeta_{\max}) = \tilde{\lambda}_0, \tag{S27}$$

where $\zeta_{max} = A/2\pi R_0^2$ is the total dimensionless membrane area .

1.3.1 Numerical implementation

We solved the system of first-order differential equations (Eq. (S26)) with boundary conditions Eq. (S27) using the finite element software COMSOL MULTIPHYSICS ® 5.3, using the "General Form PDE" module. Here, we summarize the steps and assumptions that we used for each simulation.

- All the simulations were performed for a fixed area of the membrane ($\mathrm{A_{membrane}} = 8\pi\ \mu\mathrm{m}^2$).
- The membrane patch was initialized to be a perfect cylinder ($\psi = \pi/2$) with radius R_0= 200 nm.
- The membrane domain (ζ) was discretized equally with mesh size = 0.001.
- To have a sharp but smooth transition in heterogeneous properties, we used a hyperbolic tangent function given by

$$\chi = \frac{1}{2}[\tanh(g(\zeta - a_0))], \tag{S28}$$

  where χ denoted the membrane property such as bending modulus (κ), Gaussian modulus (κ_G), or protein density (σ), g is a constant and a_0 represents the area of the heterogeneity.
- The applied tension at the boundary (λ_0) in Fig. S1, the bending modulus ratio (κ_{ratio}) in Fig. 2, and the number of proteins per unit area (σ_0) in Fig. 3 were progressively increased such that each solution was used as an initial guess for the next step.

2 Tables

2.1 Table of Notation

Table 1: Notation used in the model

Notation	Description	Units
E	Strain energy	pN · nm
γ	Lagrange multiplier for incompressibility constraint	$\mathrm{pN/nm}$
p	Pressure difference across the membrane	$\mathrm{pN/nm}^2$
σ	Protein density	nm^{-2}
C	Spontaneous curvature	nm^{-1}
θ^{ξ}	The surface coordinatwe	
W	Local energy per unit area	pN/nm
$\mathbf{r}$	Position vector	
$\mathbf{n}$	Normal to the membrane surface	unit vector
$\boldsymbol{\nu}$	Tangent to the membrane surface in direction of increasing arc length	unit vector
$\boldsymbol{\tau}$	Rightward normal in direction of revolution	unit vector
$\mathbf{a}_{\xi}$	Basis vectors describing the tangent plane	
λ	Membrane tension, $-(W+\gamma)$	pN/nm
H	Mean curvature of the membrane	nm^{-1}
K	Gaussian curvature of the membrane	nm^{-2}
κ_{ν}	Tangential curvature	nm^{-1}
κ_{τ}	Transverse curvature	nm^{-1}
κ	Bending modulus	pN · nm
κ_G	Gaussian modulus	pN · nm
s	Arc length	nm
θ	Azimuthal angle	
ψ	Angle between $\mathbf{e}_r$ and $\mathbf{a}_s$	
φ	Angle between normal vector to surface **n** and protein meridian	
α	Constant	$\mathrm{nm}^{1.5}\cdot\ \mathrm{pN}^{0.5}$
μ	Constant indicating lipid-protein moietic length scale	nm
R	Radial distance	nm
Z	Elevation from base plane	nm
$\mathbf{e}_r(\theta)$	Radial basis vector	unit vector
$\mathbf{e}_{\theta}$	Azimuthal basis vector	unit vector
$\mathbf{k}$	Altitudinal basis vector	unit vector
A	Membrane area	nm^2
s_{max}	Maximum arc length	nm
ζ_{max}	Maximum membrane area	nm^2
R_0	Radius of the cylinder	nm
a_0	Area of the heterogeneity	nm^2
L_k	Induced length scale by a rigid domain	nm
L_{σ}	Induced length scale by a protein-induced spontaneous curvature	nm
L_d	Arc length distance between two beads	nm

Table 2: Notation used in the model

Notation	Description	Units
λ_0	Surface tension at boundary	$\mathrm{pN/nm}$
σ_0	Number of proteins per unit area	nm^{-2}
L_c	Cylinder length	nm
r_c	Cylinder radius	nm
r_b	Beads radius	nm
L	Shape equation variable	nm^{-1}
x	Dimensionless radial distance	
y	Dimensionless height	
h	Dimensionless mean curvature	
c	Dimensionless spontaneous curvature	
l	Dimensionless L	
$\tilde{\lambda}$	Dimensionless surface tension	
$\tilde{p}$	Dimensionless pressure	
$\tilde{\kappa}$	Dimensionless bending modulus	
$\tilde{\kappa}_G$	Dimensionless Gaussian modulus	
$\tilde{\sigma}$	Dimensionless protein density	
$\tilde{\mu}$	Dimensionless constant μ	
$\tilde{\alpha}$	Dimensionless constant α	
G	Dimensionless Gaussian curvature	
L_c	Length of cylinder	nm
r_c	Radius of cylinder	nm
r_b	Radius of bead	nm
ζ	Dimensionless membrane area	
$A_{\text{separation}}$	Area separation between two beads	nm^2
$\mathrm{A}_{\mathrm{rigid}}$	Area of the rigid segment	nm^2
$\mathrm{A}_{\mathrm{membrane}}$	Total area of the membrane	nm^2
$\mathrm{A}_{\mathrm{protein}}$	Area of the coat protein	nm^2
κ_{lipid}	Bending modulus of the bare lipid bilayer	$\mathrm{pN} \cdot \mathrm{nm}$
κ_{rigid}	Bending modulus of the rigid segments	$\mathrm{pN} \cdot \mathrm{nm}$
κ_{ratio}	Bending rigidity ratio $\kappa_{\text{rigid}}/\kappa_{\text{lipid}}$	
$\kappa_{\mathrm{G,lipid}}$	Gaussian modulus of the bare lipid bilayer	$\mathrm{pN} \cdot \mathrm{nm}$
$\kappa_{\mathrm{G,rigid}}$	Gaussian modulus of the rigid segments	$\mathrm{pN} \cdot \mathrm{nm}$

2.2 Table of parameters

Table 3: Value of parameters used in the model for different figures

Notation	Description	Value
λ_0	Figs. 2, 3, 4A, 4B, 5, S3, S5, S4, S6, S7, S8, S9, S10	$0.064\ \mathrm{pN/nm}$
	Figs. 4C, 4D,	0.004 – $0.064\ \mathrm{pN/nm}$
	Figs. S1, S2	0 – $0.064\ \mathrm{pN/nm}$
κ_{ratio}	Figs. 3, 4C, 5B, 5D, S1, S2, S4, S5, S8, S9, S10B	1
	Figs. 2, S3	1 – 30
	Figs. 4A, S7A	11
	Figs. 4B and 4D, 5C, S7B	1 – 11
	Figs. 5E, S10C	4
	Fig. S6	2
σ_0	Figs. 3,5E, S5, S8, S10C	0 – $1.25\times10^{-4}\ \mathrm{nm}^{-2}$
	Figs. 4B and 4C, S5, 5D, S6, S7B, S10B	0 – $2.5\times10^{-4}\ \mathrm{nm}^{-2}$
	Figs. 2, 5C, S1, S2 S3, S4, S10A	0
	Fig. S9A	$0.7\times10^{-4}\ \mathrm{nm}^{-2}$
	Fig. S9B	$2.5\times10^{-4}\ \mathrm{nm}^{-2}$
α	Constant for all figures	$3.57\times10^{3}\ \mathrm{nm}^{1.5}\cdot\mathrm{pN}^{0.5}$
$\mu\varphi$	Constant for all figures	$200\ \mathrm{nm}$
A_{membrane}	All figures except Fig. S8	$8\pi\ \ \mu\mathrm{m}^2$
	Fig. S8	$17.6\pi\ \ \mu\mathrm{m}^2$
A_{rigid}	Constant for all figures	$1.6\pi\ \ \mu\mathrm{m}^2$
A_{protein}	Constant for all figures	$1.6\pi\ \ \mu\mathrm{m}^2$
$A_{\text{separation}}$	Figs. 5B, S7, S8	$1.6\pi\ \ \mu\mathrm{m}^2$
	Figs. 5C, 5D, 5E, S9, S10	0 – $1.6\pi\ \ \mu\mathrm{m}^2$
p	For all figures	0

3 Supplementary Figures

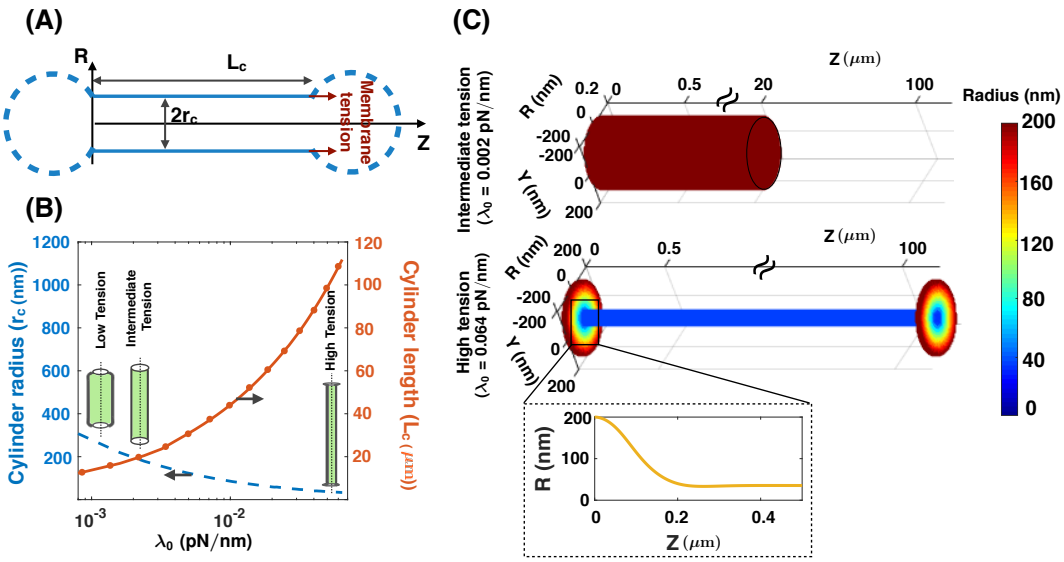

Figure S1: Tension-mediated nanotube elongation. (A) Schematic showing the simplest morphology for a nanotube, a cylinder with a radius $\mathrm{r_c}$ and length $\mathrm{L_c} = 100\mathrm{r_c}$ between two adjacent cells in the absence of both membrane cytoskeleton and osmotic pressure. (B) Tubular membrane elongation by tuning the membrane tension at the boundary. Tube radius and length are plotted as a function of applied tension at the boundary (λ_0). With increasing edge tension, the cylinder radius ($\mathrm{r_c}$) decreases but the length ($\mathrm{L_c}$) increases since the total area of the membrane is fixed. Based on the ratio of the length and radius, the observed shapes can be classified in three categories: (1) a wide and short cylinder ($\mathrm{L_c}/\mathrm{r_c} \approx 1/3$) at low tension, (2) a perfect cylinder ($\mathrm{L_c}/\mathrm{r_c} \approx 100$) at intermediate tension, and (3) a narrow and long cylinder similar to a nanotube ($\mathrm{L_c}/\mathrm{r_c} \approx 3 \times 10^3$) at high tension. (C) Radius variation in a tubular membrane versus an elongated nanotube. A perfect cylinder stabilized at an intermediate tension ($\lambda_0 = \kappa_{\mathrm{lipid}}/4\mathrm{r_c^2} = 0.002\,\mathrm{pN/nm}$) has a uniform radius ($\mathrm{r_c} = 200\,\mathrm{nm}$). In contrast, the elongated nanotube at high tension ($\lambda_0 = 0.064\,\mathrm{pN/nm}$), has large radii at the edges ($\mathrm{r_c} = 200\,\mathrm{nm}$) and a small radius along the connecting tubule ($\mathrm{r_c} = 40\,\mathrm{nm}$). The inset shows the smooth transition of the nanotube morphology at the edge boundary.

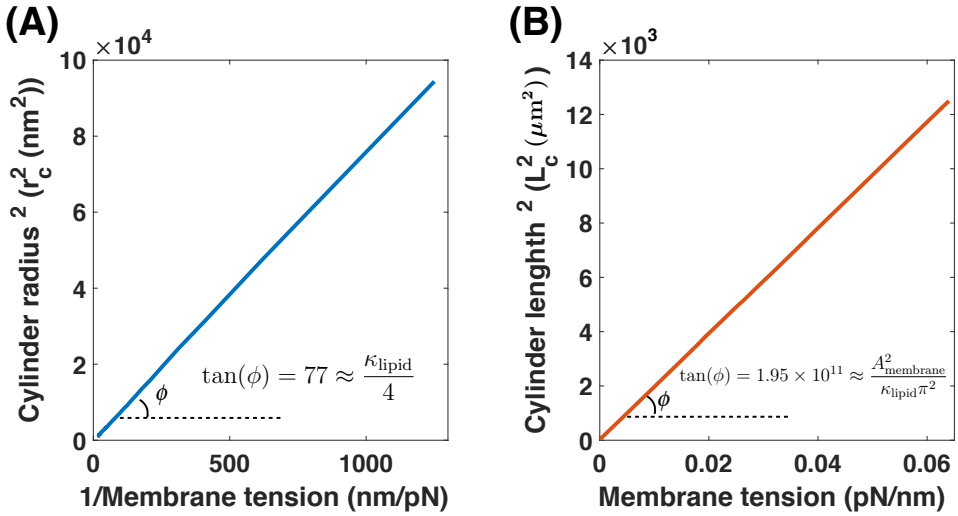

Figure S2: Cylinder radius and height as a functions of the edge membrane tension (λ_0). (A) For a homogeneous membrane ($\kappa_{\text{lipid}} = 320\,\text{pN}\cdot\text{nm}$), the square of the cylinder radius (r_c^2) is almost linearly proportional to the inverse of membrane tension (λ_0). Minimization of the Helfrich energy, while ignoring edge effects, gives an analytical expression for the radius as $\text{r}_\text{c}^2 = \kappa_{\text{lipid}}/4\lambda_0$ [14]. (B) The square of cylinder height (L_c^2) increases linearly with the membrane tension (λ_0). Ignoring the deformation at the boundaries, the total area of the membrane can be written based on the radius and height of the cylinder ($\text{A}_{\text{membrane}} = 2\pi\text{r}_\text{c}\text{L}_\text{c}$). Thus, for a fixed area of membrane, the square root of nanotube height is proportional to the applied tension according to $\text{L}_\text{c}^2 = (\text{A}_{\text{membrane}}^2/\kappa_{\text{lipid}}\pi^2)\lambda_0$.

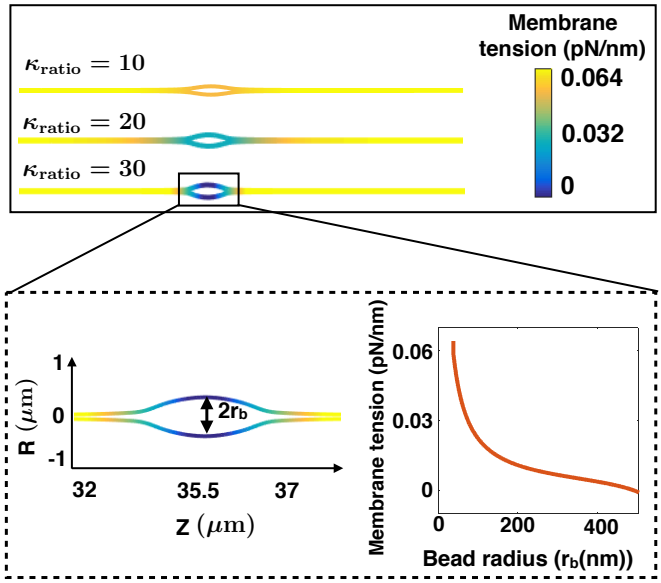

Figure S3: Membrane tension distribution along nanotubes corresponding to local bending rigidity variation shown in Fig. 2. The region of higher rigidity and bead-shaped deformations correspond to a lower membrane tension. The inset shows the reduction of the local membrane tension versus the bead radius.

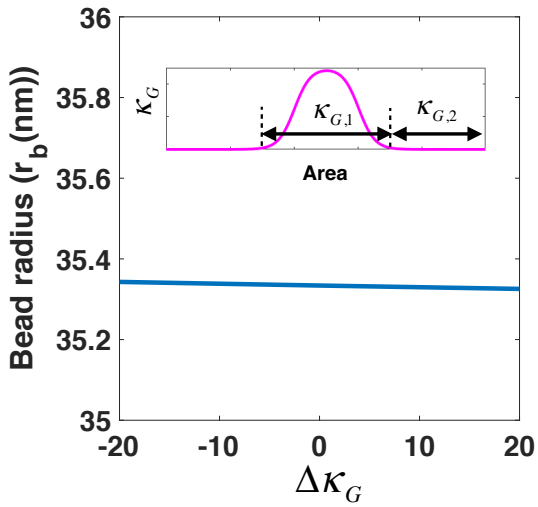

Figure S4: Beads do not form with a localized Gaussian modulus variation. Here we applied a variable Gaussian modulus splay – prescribed as a hyperbolic tangent Eq. (S28) – along a constant area of the membrane ($\mathrm{A_{Gaussian}} = 1.6\pi\ \mu\mathrm{m}^2$) at the center of the nanotube, $\lambda_0 = 0.064\,\mathrm{pN/nm}$. We define $\Delta\kappa_\mathrm{G} = (\kappa_{\mathrm{G},1} - \kappa_{\mathrm{G},2})/\kappa_\mathrm{lipid}$ varying between negative and positive values [13, 15]. There is a negligible membrane deformation with increasing the Gaussian moduli difference from $\Delta\kappa_\mathrm{G} = -20$ to $\Delta\kappa_\mathrm{G} = 20$ such that the bead radius is almost equal to the nanotube radius ($\mathrm{r_n} = 35.334\,\mathrm{nm}$) at $\Delta\kappa_\mathrm{G} = 0$.

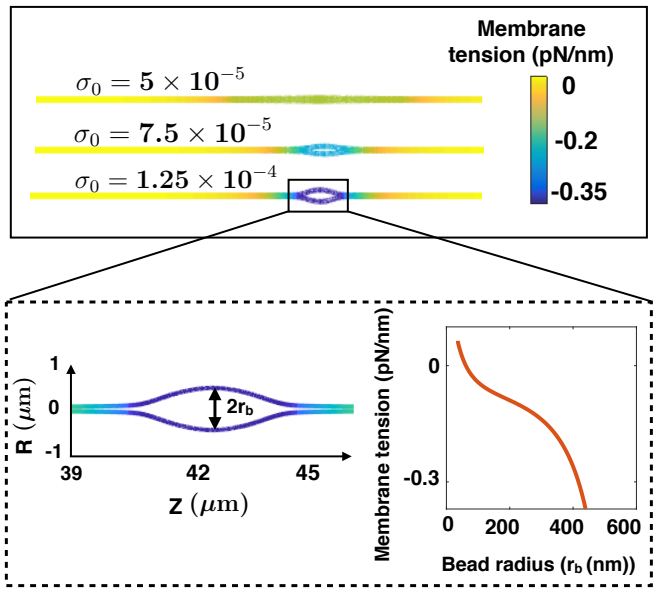

Figure S5: Membrane tension distribution along nanotubes corresponding to local protein aggregation shown in Fig. 3. The region of protein aggregation and bead-shaped deformations corresponds to a lower membrane tension. The inset shows the reduction of the local membrane tension versus the bead radius. Here the negative membrane tension can be interpreted as a surface pressure [5].

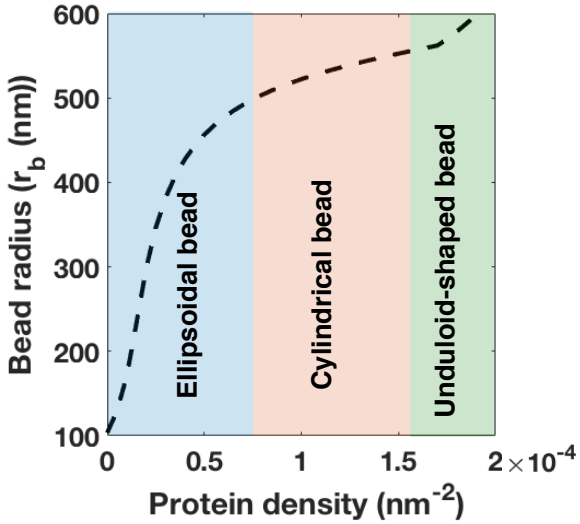

Figure S6: Bead radius as a function of the protein density for a rigid protein-enriched domain ($\kappa_{\text{ratio}} = 2$). The three different observed bead morphologies in Fig. 4 are separated with same colors. The slope of bead radius versus the protein density in cylindrical and unduloid-shaped beads is smaller compared to the ellipsoidal bead.

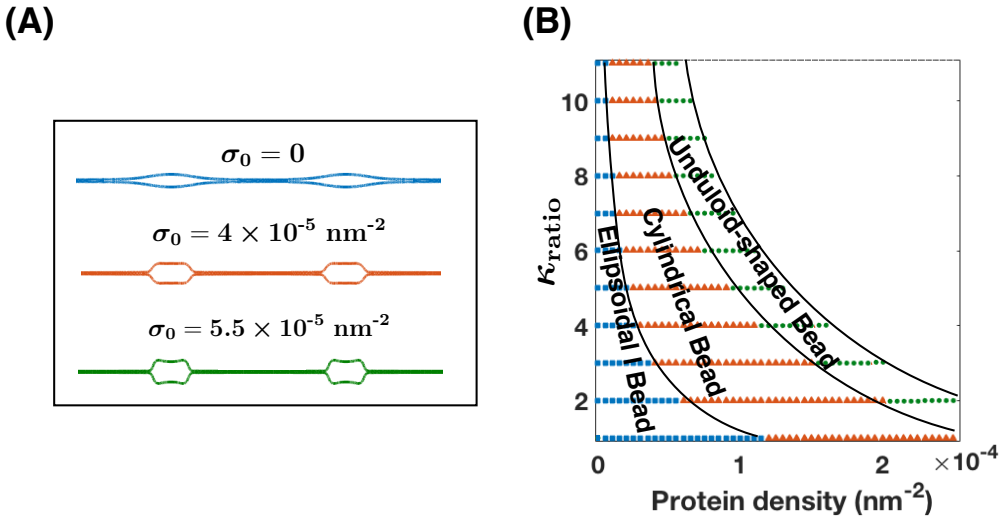

Figure S7: Formation of two beads far away from each other with no interaction. (A) Three different shapes of two beads in the presence of two rigid domains of proteins with $\kappa_{\text{ratio}} = 11$, and $\lambda_0 = 0.064\,\text{pN/nm}$. Here, we set the protein density distribution the same as Fig. 5A. Similar to a single bead (Fig. 4A), as protein density increases, each bead shape transforms independently from an ellipsoidal bead to a cylindrical one and finally a unduloid-shaped bead. (B) The bending rigidity ratio versus the number of the proteins per unit area phase diagram for $\lambda_0 = 0.064\,\text{pN/nm}$. As expected, the phase diagram is exactly same as Fig. 4B because the beads are far away from each other and therefore their shapes evolve completely independently of one another.

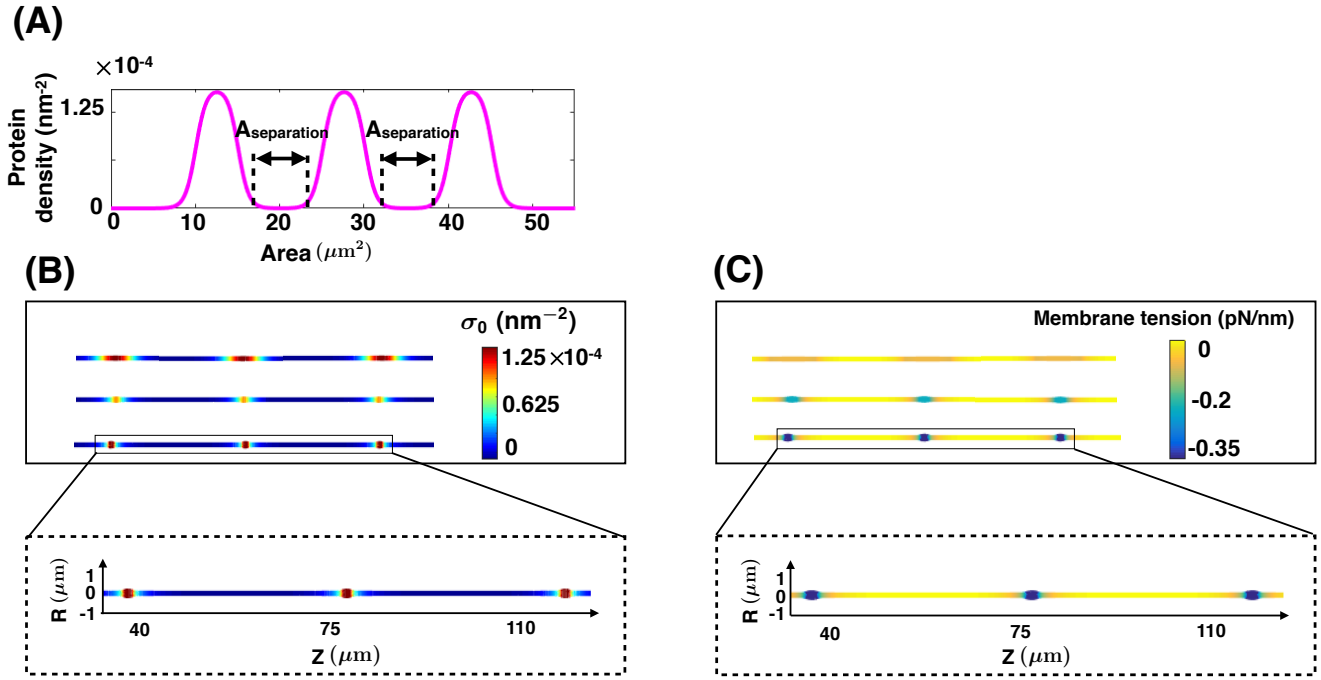

Figure S8: Formation of three beads far away from each other with no interaction. Here in order to have three domains of heterogeneity we set the total area of the membrane as $A_{\text{membrane}} = 17.6\pi\ \mu\text{m}^2$. (A) Protein density distribution with three domains of protein accumulation. The area of each protein-enriched domain is $A_{\text{protein}} = 1.6\pi\ \mu\text{m}^2$ and the domains are far from each other with $A_{\text{separation}} = 1.6\pi\ \mu\text{m}^2$. The number of proteins within each domain increases equally from $\sigma_0 = 0$ to $\sigma_0 = 1.25 \times 10^{-4}\ \text{nm}^{-2}$. (B) Three independent beads form corresponding to each protein-enriched domain. (C) Local membrane tension distribution along the nanotubes.

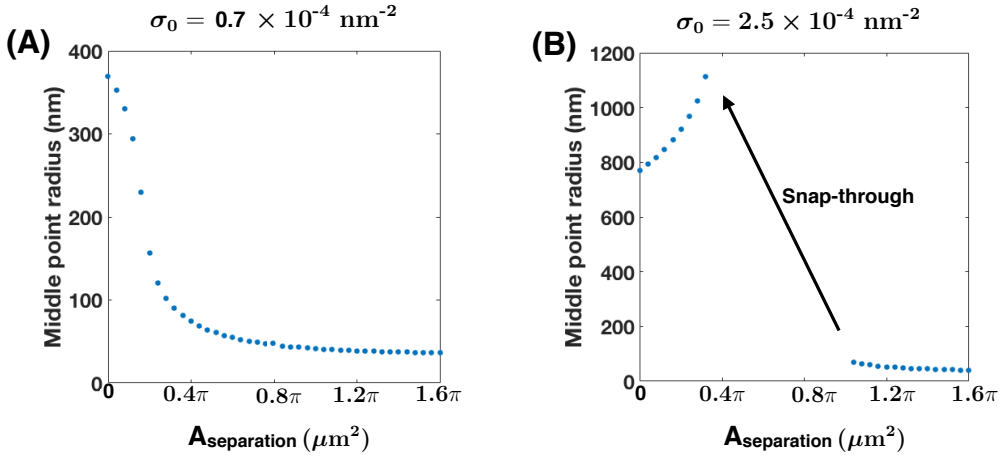

Figure S9: Transition between two beads to one bead with decreasing area separation from $A_{\text{separation}} = 4.8\ \mu\text{m}^2$ to $A_{\text{separation}} = 0$. (A) The membrane radius at the middle of nanotube – where $A_{\text{membrane}} = 4\pi\ \mu\text{m}^2$ – increases monotonically with decreasing area separation between the beads at $\sigma_0 = 0.7 \times 10^{-4}\ \text{nm}^{-2}$. (B) With decreasing area separation between two beads, initially the membrane radius at the middle increases and then suddenly jumps to almost 1200 nm with formation of one bead at $\sigma_0 = 2.5 \times 10^{-4}\ \text{nm}^{-2}$. The radius of the middle point decreases after snap-through transition.

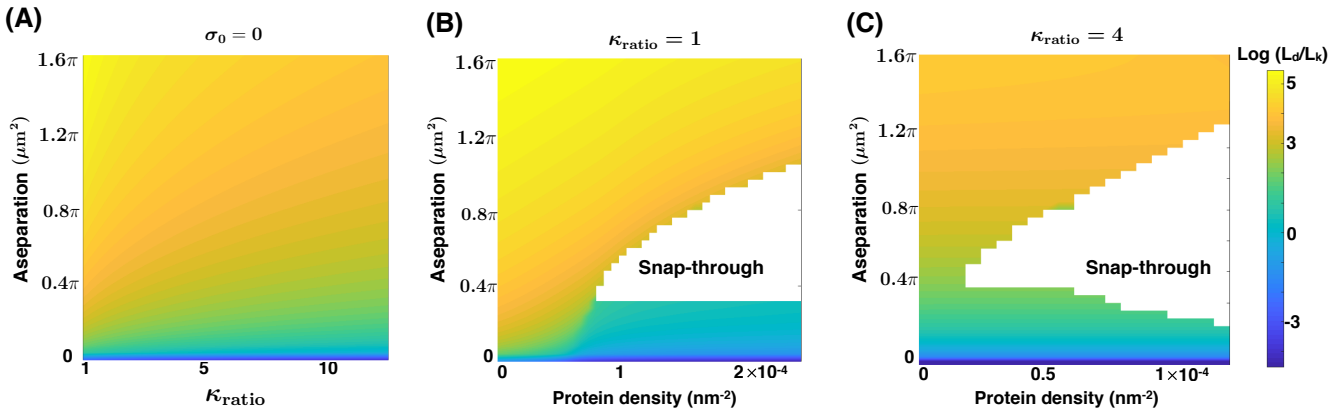

Figure S10: Length scale competition determines the minimal distance between beads before they overlap. In Fig. 5C we varied the the area separation between the beads as an independent parameter. By using Eg. S23, we can covert this area separation to arc length ($\mathrm{L_d}$). (A) Contour plot of the Log of the $\mathrm{L_d}/\mathrm{L_k}$ ratio for $A_{\text{separation}}$ varying between 0 and $1.6\pi\ \mu\mathrm{m}^2$ as a function of the bending rigidity ratio κ_{ratio}. We find that the transition from two beads to one bead with decreasing the distance between domains occurs when the arc length distance $\mathrm{L_d}$ is one order of magnitude smaller than the induced length scale $\mathrm{L_k}$. (B) Contour plot of the Log of the $\mathrm{L_d}/\mathrm{L_k}$ ratio as a function of protein density and area separation between beads for a homogeneous membrane $\kappa_{\text{ratio}} = 1$. As expected, the green and blue regions, where $\mathrm{Log}(\mathrm{L_d}/\mathrm{L_k}) \leq 1$, overlap with the one bead region in Fig. 5D. However, the yellow region with $\mathrm{Log}(\mathrm{L_d}/\mathrm{L_k}) > 1$ corresponds to the two beads configuration in Fig. 5D. (C) Contour plot of the Log of the $\mathrm{L_d}/\mathrm{L_k}$ ratio as a function of protein density and area separation between beads assuming that the bending rigidity along the protein domain is 4 times larger than the bare lipid membrane ($\kappa_{\text{ratio}} = 4$).

References

1. D. Steigmann, "Fluid films with curvature elasticity," *Archive for Rational Mechanics and Analysis*, vol. 150, no. 2, pp. 127–152, 1999.

2. D. Steigmann, E. Baesu, R. E. Rudd, J. Belak, and M. McElfresh, "On the variational theory of cell-membrane equilibria," *Interfaces and Free Boundaries*, vol. 5, no. 4, pp. 357–366, 2003.

3. D. J. Steigmann, "Mechanics and physics of lipid bilayers," in *The Role of Mechanics in the Study of Lipid Bilayers*, pp. 1–61, Springer, 2018.

4. P. Rangamani, A. Agrawal, K. K. Mandadapu, G. Oster, and D. J. Steigmann, "Interaction between surface shape and intra-surface viscous flow on lipid membranes," *Biomechanics and modeling in mechanobiology*, pp. 1–13, 2013.

5. P. Rangamani, K. K. Mandadap, and G. Oster, "Protein-induced membrane curvature alters local membrane tension," *Biophysical journal*, vol. 107, no. 3, pp. 751–762, 2014.

6. A. Agrawal and D. J. Steigmann, "A model for surface diffusion of trans-membrane proteins on lipid bilayers," *Zeitschrift fur Angewandte Mathematik und Physik (ZAMP)*, vol. 62, no. 3, pp. 549–563, 2011.

7. T. Belay, C. I. Kim, and P. Schiavone, "Bud formation of lipid membranes in response to the surface diffusion of transmembrane proteins and line tension," *Mathematics and Mechanics of Solids*, p. 1081286516657684, 2016.

8. L. Landau, "Em lifshitz fluid mechanics," *Course of Theoretical Physics*, vol. 6, 1959.

9. W. Helfrich, "Elastic properties of lipid bilayers: theory and possible experiments," *Zeitschrift fur Naturforschung C*, vol. 28, no. 11-12, pp. 693–703, 1973.

10. M. Chabanon and P. Rangamani, "Gaussian curvature directs the distribution of spontaneous curvature on bilayer membrane necks," *Soft Matter*, 2018.

11. A. Agrawal and D. J. Steigmann, "Modeling protein-mediated morphology in biomembranes," *Biomechanics and modeling in mechanobiology*, vol. 8, no. 5, pp. 371–379, 2009.

12. A. Agrawal and D. J. Steigmann, "Boundary-value problems in the theory of lipid membranes," *Continuum Mechanics and Thermodynamics*, vol. 21, no. 1, pp. 57–82, 2009.

13. J. E. Hassinger, G. Oster, D. G. Drubin, and P. Rangamani, "Design principles for robust vesiculation in clathrin-mediated endocytosis," *Proceedings of the National Academy of Sciences*, vol. 114, no. 7, pp. E1118–E1127, 2017.

14. I. Derenyi, F. Julicher, and J. Prost, "Formation and interaction of membrane tubes," *Physical review letters*, vol. 88, no. 23, p. 238101, 2002.

15. T. Baumgart, S. Das, W. Webb, and J. Jenkins, "Membrane elasticity in giant vesicles with fluid phase coexistence," *Biophysical journal*, vol. 89, no. 2, pp. 1067–1080, 2005.